

1 **Single-cell RNA sequencing reveals stromal evolution into LRRC15⁺**
2 **myofibroblasts as a determinant of patient response to cancer immunotherapy**

3
4
5 Claudia X. Dominguez^{1*}, Sören Müller^{2*}, Shilpa Keerthivasan¹, Hartmut Koeppen³,
6 Jeffrey Hung³, Sarah Gierke⁴, Beatrice Breart¹, Oded Foreman³, Travis W. Bainbridge⁵,
7 Alessandra Castiglioni¹, Yasin Senbabaoglu², Zora Modrusan⁶, Yuxin Liang⁶, Melissa R.
8 Junttila⁷, Christiaan Klijn², Richard Bourgon² & Shannon J. Turley^{1,#}

9
10
11 Departments of ¹Cancer Immunology, ²Bioinformatics and Computational Biology,
12 ³Pathology, ⁴Center for Advanced Light Microscopy, ⁵Protein Chemistry,
13 ⁶Microchemistry, Proteomics & Lipidomics, and ⁷Translational Oncology, Genentech,
14 South San Francisco, California

15
16 *Equal contribution #Corresponding author

17
18 Corresponding Author: Shannon J. Turley, Genentech, 1 DNA Way, South San
19 Francisco, CA 94080, USA. Phone: (650)-225-2790 E-mail: turley.shannon@gene.com

20
21 **Disclosure of Potential Conflicts of interest**

22 All authors are employees and all but C.X.D. are stockholders of Genentech/Roche.
23 Otherwise authors declare no competing interests.

24
25 **RUNNING TITLE**

26 Characterization of TGFB-activated LRRC15+ CAFs in PDAC

27

28 **ABSTRACT**

29 With only a fraction of patients responding to cancer immunotherapy, a better
30 understanding of the entire tumor microenvironment is needed. Using single-cell
31 transcriptomics we chart the fibroblastic landscape during pancreatic ductal
32 adenocarcinoma (PDAC) progression in animal models. We identify a population of
33 carcinoma-associated fibroblasts (CAFs) programmed by transforming growth factor
34 beta and expressing the leucine-rich repeat containing 15 (LRRC15) protein. These
35 LRRC15⁺ CAFs surround tumor islets and are absent from normal pancreatic tissue.
36 The presence of LRRC15⁺ CAFs in human patients was confirmed in >80,000 single-
37 cells from 22 PDAC patients as well as immunohistochemistry on samples from 70
38 patients. Furthermore, immunotherapy clinical trials comprising over 600 patients across
39 6 cancer types revealed elevated levels of the LRRC15⁺ CAF signature correlated with
40 poor response to anti-PD-L1 therapy. This work has important implications for targeting
41 non-immune elements of the tumor microenvironment to boost responses of cancer
42 patients to immune checkpoint blockade therapy.

43

44

45 **SIGNIFICANCE**

46

47 This study describes the single-cell landscape of cancer-associated fibroblasts in
48 pancreatic cancer during in vivo tumor evolution. A TGFB-driven, LRRC15⁺ CAF lineage
49 is associated with poor outcome in immunotherapy trial data comprising multiple solid
50 tumor entities and represents a target for combinatorial therapy.

51

52 INTRODUCTION

53 Pancreatic ductal adenocarcinoma (PDAC) remains a devastating disease, with
54 a 5-year survival rate of 7%(1). One of the hallmarks of this aggressive cancer is a
55 dramatic desmoplasia driven by carcinoma-associated fibroblasts (CAFs). CAFs not
56 only deposit the extracellular matrix (ECM) that characterizes desmoplasia, but also
57 produce factors that promote tumor growth. Subsequently, CAFs have been targeted in
58 efforts to improve PDAC outcomes, with conflicting results(2–6). The discrepancy in
59 outcomes might be explained by CAF heterogeneity, with different fibroblast populations
60 having separate, perhaps even opposing functions(7,8). Smooth muscle actin (SMA)
61 and fibroblast activating protein (FAP) have been described as showing heterogenous
62 expression on CAF populations(8,9) and SMA high CAFs have further been identified
63 as a tumor adjacent transforming growth factor beta (TGFB) driven population with
64 different inflammatory properties from SMA low CAFs.

65 Intriguingly, despite the conflicting results of targeting CAFs as a single therapy,
66 modulating CAFs in combination with immunotherapies improved outcomes in several
67 preclinical models(2,4,10). As these studies model cancers that show resistance to
68 immunotherapies alone, they suggest that elucidating CAF functions may provide the
69 understanding needed to design more efficacious immunotherapeutic approaches and
70 address the unmet clinical need in devastating cancers like PDAC. The full scope of
71 CAF functions in the context of cancer immunotherapy remain to be determined, but will
72 necessarily be influenced by the fibroblast state at the tissue-tumor interface.

73 We sought to provide an unbiased assessment of fibroblast heterogeneity in
74 normal as well as PDAC tissues by using a combination of bulk and single-cell RNA-seq
75 of stromal cells. Normal tissues, non-malignant adjacent, early and advanced tumors
76 from genetically engineered mouse models (GEMMs) were utilized in this study. We
77 hypothesized that the changing microenvironment during tumor progression impacts the
78 phenotype of resident tissue fibroblasts resulting in their development into multiple CAF
79 subsets. Our analyses revealed that pre-existing fibroblast heterogeneity in normal
80 tissue dictated the developmental trajectories of murine CAFs. These data enabled
81 identification of the transcriptional profiles of individual CAF populations, and revealed a
82 TGFB programmed CAF, identifiable by expression of leucine rich repeat containing 15

83 (LRRC15), that became the dominant fibroblast in advanced tumors. Combining publicly
84 available human sequencing data with newly acquired immunohistochemistry of 70
85 PDAC patients, we confirmed the identification of these LRRC15⁺ CAFs in human
86 patients. The LRRC15⁺ CAF signature was used to evaluate their impact on anti-PDL1
87 immunotherapy response in large patient cohorts and revealed that high expression of
88 the LRRC15⁺ CAF signature was associated with poor response to anti-PD-L1 therapy
89 in immune excluded tumors.

90

91 RESULTS

92 ***PDPN⁺ cells are the dominant fibroblast population in normal and PDAC murine*** 93 ***pancreas***

94 To characterize the stromal compartment in PDAC we began by optimizing
95 digestion conditions for stromal cell phenotyping from murine pancreas, starting with
96 protocols to isolate the dominant known stromal cell in the pancreas, the stellate cell.
97 Standard stellate cell pronase-based digestion(11) was observed to cleave many
98 surface markers whereas our novel digestion method preserved podoplanin (PDPN)
99 and platelet endothelial cell adhesion molecule-1(PECAM-1/CD31) expression (Fig. 1a).
100 To model PDAC we used the *Pdx1^{cre/+};LSL-Kras^{G12D/+};p16/p19^{flox/flox}* (KPP) mice which
101 form aggressive tumors within 12 weeks(12). While tumors from these mice often show
102 several different carcinoma types including sarcomatoid, acinar, and mucinous
103 subtypes, we observe up to 88% of a given cohort develop substantial regions of PDAC
104 as has been previously reported(13,14) (Suppl. Fig. 1a). Flow cytometry of dissociated
105 pancreases from the KPP mice and normal mice from the same albino B6
106 background(B6(Cg)-Tyrc-2J/J) revealed 3 major populations of stromal cells with similar
107 composition between the two states (Fig.1b and Suppl. Fig. 1b). CD31⁺ stromal cells
108 were predominantly PDPN- blood endothelial cells with very few lymphatic endothelial
109 cells(15). The remaining CD31⁻ cells were largely PDPN⁺ with fibroblast and stellate cell
110 characteristics (Fig. 1b, Suppl. Fig. 1c-f). Immunofluorescence microscopy confirmed
111 the presence of PDPN⁺ cells around structures in the normal pancreas including acinar
112 clusters, ducts, and islets as well as a single cell layer of mesothelial cells encapsulating
113 the pancreas (Fig. 1c [left] and Suppl. Fig. 1g). The KPP mice exhibited increased

114 PDPN expression, most dramatically bordering tumor islets, but also in some areas
115 distal to tumors (Fig. 1c [middle and right] and Suppl. Fig. 1h). To better characterize
116 changes in the non-endothelial stroma with tumor progression, we harvested tissues
117 from normal mice, mice with early tumors (<5mm), and mice with advanced disease
118 (tumors>5mm). Pancreatic stromal cells were sorted on CD31⁻PDPN⁺PDGFRA⁺ and
119 CD31⁻PDPN⁻ (DN) cells for RNA sequencing of these two populations. This strategy
120 was used to exclude mesothelial cells, which are also PDPN⁺ but negative for PDGFRA
121 (16) (Suppl. Fig. 1i). The transcriptional profiles confirmed that PDPN⁺ stromal cells are
122 enriched for fibroblast signature genes and the DN population for pericyte signature
123 genes(17) (Fig. 1d). Several CAF associated genes were enriched in the PDPN⁺ PDAC
124 population, although in mice *Fap*, *Sma (Acta2)*, *Fsp1*, and *Pdgfrb*, often described as
125 CAF marker genes, were detected to some degree in both stromal populations in
126 normal and PDAC pancreas. Particularly, we find that *Acta2* is highest in normal
127 pericytes and *Fap* is equally high in normal fibroblasts (Fig. 1e). While the pericyte
128 enriched population also showed changes between normal and tumor tissues, we
129 focused on the PDPN⁺ populations as they represent the major CAF constituent.

130

131 **Single-cell RNA-seq identifies several populations of PDPN⁺ cells**

132 While PDPN⁺ stromal cells constituted the majority of CAFs, they expressed
133 individual CAF markers at variable levels between replicates (e.g. *Il6* levels ranged from
134 60 to 240 Reads Per Kilobase of Transcript per Million mapped reads [rPKM]), and
135 furthermore they appeared to simultaneously express markers reported to separate
136 CAF subsets *i.e.* *Acta2* and *Il6* (Fig. 1e). This implied a significant heterogeneity within
137 the PDPN⁺ stroma. To resolve this heterogeneity, we performed single-cell RNA-
138 sequencing (scRNA-seq) of viable PDPN⁺ stromal cells from the pancreas of KPP and
139 normal mice. To better capture changes that occur with tumor progression we divided
140 the KPP samples into tumor-adjacent tissue, as well as small (1-4mm), and large (5-10
141 mm) tumor samples for scRNA-seq (Fig. 2a). Five animals were pooled per condition in
142 each of two biological replicates and scRNA-seq was performed (Fig. 2a). After quality
143 control and batch correction (Suppl. Fig. 2a, described in Methods) we obtained 13,454
144 high-quality cells for downstream analysis (replicate 1: n=3,315; replicate 2: n=10,139).

145 Graph-based clustering of cells after dimensionality reduction with t-Distributed
146 Stochastic Neighbor Embedding (t-SNE) (Fig. 2b) or Uniform Manifold Approximation
147 and Projection (UMAP, Suppl. Fig. 2b), identified 12 robust groups of cells (Suppl. Table
148 1).

149 Endothelial, myeloid, and acinar cell clusters represent contaminating cells as
150 anti-CD31, -CD45, and -EPCAM, respectively, were used to gate out those populations
151 in our flow protocol prior to sequencing (3% of all cells, Fig. 2a-c and Suppl. Fig. 2c).
152 Within the remaining 97% of cells, 83.5% of cells were identified as fibroblasts, 11.5%
153 were classified as tumor cells undergoing EMT, and 5.1% were mesothelial cells. All
154 clusters were represented in both replicates (Fig. 2b-d). Clusters 5 and 7 had lost
155 *Epcam* expression but retained higher expression of several keratins and genes
156 associated with an epithelial origin. This suggested they might be EMT tumor
157 populations (Suppl. Fig. 2d). To confirm this assignment, we identified *Alcam* as a gene
158 uniquely expressed by these clusters (Fig. 2c). Flow cytometry confirmed ALCAM
159 protein was expressed by a subset of cells found only in some large tumors. Isolation
160 and sequencing of ALCAM⁺ cells revealed expression of the KRASG12 allele with 98%
161 variant allele frequency (Suppl. Fig. 2e), confirming their identity as tumor cells. Cluster
162 6 was identified as mesothelial cells based on previous work from Buechler, et al. who
163 transcriptionally profiled these cells and their transcriptional differences to fibroblasts
164 using bulk RNAseq, as well as Xie et al. who identified their signature genes with
165 scRNA-seq (16,18). Genes identified by both studies as mesothelial cell markers were
166 strongly enriched in cluster 6, conversely 18 of the 20 most enriched genes in cluster 6
167 were also upregulated in mesothelial cells compared to fibroblasts in the Buechler et al.
168 dataset (Fig. 2c and 2e, Suppl. Table 2). We primarily observed mesothelial cells in
169 normal, and normal adjacent tissues (Fig. 2d).

170 Clusters 0-4, 8 and 9 were identified as fibroblasts by their expression of
171 signature fibroblast genes (Suppl. Fig. 2d). Two clusters of normal tissue fibroblasts
172 (ntFib) derived from normal mice (c3 and c4), as well as five clusters of CAFs were
173 identified (Fig. 2b and Suppl. Fig. 2b; c0, c1, c2, c8, and c9). C0 and c1 were most
174 abundant in tissue adjacent to tumors (~88% of CAFs; Fig. 2f). Meanwhile, the
175 frequency of cells from c8 and especially c2 increased with tumor progression and

176 dominated in late stage tumors (>70% of all CAFs) (Fig. 2f). Given the disappearance of
177 ntFib with tumor progression but proximity of normal fibroblast and CAF clusters in tSNE
178 and UMAP space, we hypothesized that heterogeneity at baseline might play a role in
179 subsequent CAF development.

180

181 ***In mouse two separate fibroblast lineages co-evolve during tumor progression***
182 ***driven by TGFB and IL1***

183 UMAP dimensionality reduction of ntFib alone confirmed two major *Pdgn*⁺*Pdgfra*⁺
184 cell populations (Fig. 3a), and we identified their transcriptional profiles (Suppl. Fig. 3a
185 and Suppl. Table 3). The c3 population expressed ECM genes associated with elastin
186 fibrils and ECM attachment (i.e. *Emilin2*, *Mfap5*, *Fbn1*) while the c4 population was
187 characterized by high expression of ECM proteins that suggested a predominant role in
188 structural support through the production and maintenance of collagen networks and
189 basement membranes (i.e. *Col4a1*, *Col6a6*, *Plc*). Consequently, c4 exhibited a
190 significantly higher overall expression of collagens compared to c3 (Wilcoxon's rank-
191 sum test <0.001, Suppl. Fig. 3b). A similar trend was observed with respect to immune
192 regulation, with c4 showing enrichment of several immune chemo-attractants (including
193 *Ccl11*, *Cxcl14* and *Cxcl16*), while c3 showed enrichment of different immunoregulatory
194 genes (*Thbd*, *CD55*, *Il33*, *Dpp4*, and *Ackr3* [*Cxcr7*]). Their expression of non-
195 overlapping genes indicates complementary activities of c3 and c4. Flow cytometry for
196 dipeptidyl peptidase 4 (DPP4) and LY6C, markers for c3, and endoglin (ENG), a c4
197 marker (Suppl. Table 3), confirmed that both these populations can be phenotypically
198 identified (Fig. 3b).

199 To assess the transcriptional changes during tumor progression, we first
200 performed an unbiased principal component analysis (PCA) comprising all CAF and
201 ntFib cells. PC1, the component explaining the strongest variance in the dataset, clearly
202 separated c4 ntFib and c1 and c2 CAFs from c3 ntFib and c0 and c8 CAFs (Fig. 3c,
203 top). Genes driving this unbiased separation were the same found in the supervised
204 differential expression test between the two ntFibs c3 and c4 (Fig. 3c, bottom). This
205 analysis strongly suggests a lineage relationship between CAFs and pre-existing
206 fibroblasts in the tissue. To investigate this further, we calculated a score for each CAF

207 cell based on the normal fibroblast ontogeny signature genes (Suppl. Fig. 3c) which
208 enabled tracing of the CAF populations back to their non-malignant ancestor (Fig. 3d,
209 Suppl. Fig. 3c). C3 and c4 ntFibs have separate differentiation trajectories during tumor
210 progression with c4 giving rise to c1 CAFs, which predominantly gives rise to c2 CAFs,
211 meanwhile, c3 ntFibs give rise to c0 CAFs, which then predominantly progress into c8
212 CAFs (Fig. 3d, right, Fig. 3e). We find c9, strongly characterized by high expression of
213 proliferation markers (*Mki67*, *Top2a*), splits into two clusters in UMAP space (Suppl. Fig.
214 2b), one aligning with EMT tumor cells, the other one aligned with c2 CAFs. The
215 proliferating, CAF-proximal cells also exhibit a higher c4 ntFIB score, explaining the
216 observed expansion of descendants of this lineage with tumor progression (Suppl. Fig.
217 3d). We thus conclude that non-tumor cells from c9 are mostly a proliferating subset of
218 c2 CAF.

219 The trajectories for the two separate fibroblast populations were confirmed with
220 pseudo time analysis for each of the lineages(19) (Fig. 3f). Comparing the expression of
221 ECM genes and selected immune regulatory genes across all of the CAF clusters
222 revealed a sharp transcriptional shift in the programming of c2 and c8 (Fig. 3g). In the
223 transition from c4 ntFib there is a significant loss of basement membrane components
224 (i.e. Type IV and Type VI collagens) with a drastic increase in levels of several fibrillar
225 collagens in c2 (Fig. 3g), indicating an increase and reorganization of fibrillar collagen
226 deposition(20,21). CAFs originating from c3 also increase expression of ECM genes,
227 particularly fibrillar collagens (Fig. 3g, top), but the most dramatic changes observed
228 with tumor progression are in chemokine and cytokines expression (Fig. 3g, bottom)
229 such as the upregulation of *Cxcl9/10*, *Cxcl1*, and *Ccl2* which likely recruit myeloid
230 populations through *Cxcr2* and *Ccr2* as well as pleiotropic cytokines such as *Il6*(22–24),
231 particularly in late stage fibroblasts (Fig. 3g). Interestingly, while there are differences in
232 expression levels between c2 and c8 CAFs we also see increased expression of genes
233 encoding factors that are known to support tumor cell survival and metastasis, such as
234 *Timp1*, *Vegf*, *Il11*, *Lif*, and *Pdgf*(25–29) that are increased in both lineages (Fig. 3g).
235 Moreover, with tumor progression both lineages acquire potential immune regulatory
236 gene expression such as increased *Mif* and *Timp1* which can drive infiltration of
237 myeloid-derived suppressor cells and regulatory T cells (Tregs) in PDAC(30,31). Thus,

238 while each lineage does appear to have specialized functions reflected by differences in
239 their gene signatures they also share some common programming.

240 To further investigate the signals driving the differences between the two
241 lineages, we queried the promoters of their signature genes (Suppl. Table 1) for
242 transcription factor binding sites. This analysis revealed a strong enrichment of NFKB
243 binding sites in the promoters of c8-specific genes while c2-specific genes showed
244 Smad3 binding site enrichment (Fig. 3h). Pathway enrichment analysis supported these
245 predictions, suggesting signaling through IL1 and TNFa as a driver of the c8
246 transcriptional signature and TGFB-driven activation of c2 (Fig. 3h). Furthermore, we
247 observed a strong enrichment of a TGFB fibroblast gene signature(32) in c2 cells further
248 validating TGFB as a key driver of the c2 phenotype (Fig. 3i, left). Interestingly, their
249 transcriptional signatures suggest these populations may promote their own
250 programming; while c8 cells express Il1a and their chemotactic profile suggests
251 paracrine interactions with myeloid cells, that can also be a primary source of Il1 and
252 TNF (Fig. 3i, right)(33–35), c2 shows expression of *TGFB1* and *TGFB3* (Fig. 3i).

253 To confirm the validity of our fibroblast evolution model, we compared our
254 expression signatures to the previously published fibroblast-enriched data from KPC
255 mice(36). UMAP clustering identified a group of *Pdpr*⁺ *Pdgfra*⁺ cells, that could be
256 dissected into three different sub-clusters (Suppl. Fig. 3e): one cluster of *Ly6a/c1*⁺ cells,
257 previously described as “iCAFs”, one cluster of *Col15a1*⁺ cells previously described as
258 “myCAFs”, and one cluster with high levels of *Cd74*, *H2-Ab1* and *Saa3*, previously
259 described as “apCAFs”. When we compared the average expression levels of our two
260 normal fibroblast lineage programs to these clusters, we found that myCAFs clearly
261 clustered with our c4 fibroblasts and iCAFs with c3 fibroblasts, confirming that the
262 lineage hierarchy is similarly present in the KPC model (Fig. 3j). Notably, apCAFs
263 clustered with c6 mesothelial cells from normal pancreas (Markers: Suppl. Table 3).
264 Accordingly, the Il1 c8 CAFs exhibited most similar expression profiles to iCAFs, the
265 TGFB c2 CAFs clustered with myCAFs, and the c6 mesothelial cells with apCAFs
266 (Suppl. Fig. 3f).

267

268 ***Mouse models of PDAC identify LRRC15 as a marker of TGFB driven c2 CAFs***

269 We were particularly interested in further characterizing c2 as it increased with
270 tumor progression, dominating the CAF compartment in late stage tumors (Fig. 2f), and
271 because TGFB-associated stroma is correlated with poor prognosis(32,37). Therefore,
272 we sought to identify markers that distinguish TGFB driven c2 CAFs from the other
273 fibroblast stromal subsets in PDAC. Bulk RNA-seq data from early and late stage tumor
274 PDPN⁺ CAFs identified leucine rich repeat containing 15 (*Lrrc15*) to be one of the most
275 differentially expressed genes between CAFs and ntFIBs (Fig. 4a). *Lrrc15* encodes a
276 transmembrane domain containing molecule expressed in the stroma of several human
277 tumors and upregulated by TGFB(38). Cross-referencing genes enriched in the TGFB
278 driven c2 to an atlas of proteins experimentally identified to be on the cell surface(39)
279 further validated *Lrrc15* to be a strongly enriched c2 gene encoding a surface protein
280 (Suppl. Fig. 4a).

281 The presence of LRRC15⁺ PDPN⁺ cells with fibroblast morphology in tumor
282 bearing pancreases was confirmed by immunofluorescence microscopy; LRRC15⁺ cells
283 were usually found in nests throughout the tumor-bearing pancreas surrounding tumor
284 cells in KPP GEMMs (Fig. 4b). We further employed subcutaneous models of PDAC,
285 using a cell line derived from KPP GEMMs (KPP14388). Characterization of flank
286 injections of 100k tumor cells showed tumors with similar stromal composition to the
287 KPP mice (Suppl. Fig. 4b). Immunofluorescence microscopy revealed abundant
288 LRRC15⁺ PDPN⁺ cells in the subcutaneous tumors derived from KPP PDAC line (Fig.
289 4c). Flow cytometry analysis showed that LRRC15 marked a significant portion of
290 PDPN⁺ stromal cells, and was largely absent from other cell populations in the TME
291 (Fig. 4d). Notably, LRRC15, unlike many other CAF markers, is also absent in lymph
292 node stroma as well as normal pancreas (Suppl. Fig. 4c).

293 Due to their proximity to tumor islets we decided to assess whether LRRC15⁺
294 CAFs can directly enhance tumor growth. We generated a KPP line expressing
295 Diphtheria Toxin Receptor (DTR), that allowed us to remove residual tumor cells and
296 culture isolated CAFs with the addition of DT. 2000 KPP-mApple tumor cells were
297 grown alone or in coculture with LRRC15⁺ CAFs compared to LRRC15⁻ LY6C⁺ CAFs or
298 c3 and c4 ntFIBs and assessed for their ability to promote spheroid growth in 3D
299 culture. Tumor spheroids cultured with any fibroblast population grew larger than those

300 in media alone. This demonstrated that all the fibroblasts tested can directly enhance
301 tumor growth (Fig. 4e). Although we cannot rule out that the spheroids themselves
302 reprogrammed the fibroblasts as has been previously reported(40), it suggests that the
303 specific *in situ* positioning of LRRC15⁺ CAFs next to tumor islets might be one of the
304 keys to their role in a protumor niche rather than a unique ability to promote tumor
305 growth. This experiment also represents a single functional test; given the unique
306 transcriptional differences between the fibroblasts populations we might expect
307 functional differences in other areas, such as immune regulation.

308

309 ***LRRC15⁺ CAFs are present in human PDAC samples***

310 To translate our findings from mouse models into human cancer, we re-analyzed
311 data from a recently published study of single-cell RNA-seq of human PDAC patients by
312 Peng, J. *et al.* (41). After quality control and filtering we retained 84,276 cells from 22
313 patients for downstream analysis. Clustering in dimensionality-reduced space revealed
314 12 clusters of 11 main cell types (Fig. 5a, Suppl. Table 4). All clusters were comprised
315 of cells from more than 8 patients (Fig. 5b). To confirm our tumor-cell assignment and
316 by extension ensure our fibroblast assignment did not include tumor cells that had
317 undergone EMT, we collected three independent lines of evidence. First, we confirmed
318 only cells in cluster 0 were positive for mRNA with the KRAS G12 missense mutation
319 (Fig. 5a). Second, re-analysis of a separate publicly available microdissection study(42)
320 showed that only markers for tumor cells (cluster 0) are enriched in bulk RNA-seq of
321 microdissected tumor samples compared to samples from microdissected stroma or
322 non-malignant control pancreas (Fig. 5c). Third, we identified large-scale copy number
323 variants in cells from cluster 0 but not cells from the CAF cluster (Suppl. Fig. 5a).

324 After confirming the non-tumor origin of the population identified as CAF cells, we
325 specifically focused on this cluster. Sub-clustering of the 8,931 fibroblasts revealed 3
326 distinct subsets (Suppl. Table 5): 52% of cells expressed high levels of TGFB c2 CAF
327 markers *TAGLN* and *LRRC15*, 3% were strongly enriched in IL1 c8 CAF markers *HAS1*
328 and *CCL2* (Fig. 5d), and 44% of cells expressed high levels of *C7* and *CFD*. *LRRC15*
329 was also highly expressed in the bulk RNA-seq from microdissected stroma compared
330 to tumor or normal control samples, suggesting that this population is prominent in

331 PDAC stroma (Fig. 5e). Conversely, we found *HAS1* lowly expressed across tumor,
332 stroma, and non-malignant samples and enriched in only a small fraction of
333 microdissected stroma samples, likely representing only a minor population in PDAC
334 stroma. These trends were confirmed when the average expression of signature genes
335 for each of the human fibroblast single-cell clusters was compared within the
336 microdissected bulk-seq samples (Fig. 5f). To confirm protein expression of LRRC15 in
337 human CAFs we performed dual Immunohistochemistry on 70 PDAC patients (Suppl.
338 Table 6) for LRRC15 and CD8. We found 100% of patients showed LRRC15 staining in
339 non-normal areas of pancreas and LRRC15 appeared fibrillar and was largely excluded
340 from tumor islets. Mostly, it was found surrounding them, additionally it was frequently
341 seen in proximity to CD8 T cells in the area (Fig.5g and Suppl. Fig.5b). Flow cytometry
342 on 4 patient samples further confirmed LRRC15 was largely restricted to the EPCAM⁺
343 CD45⁻ stromal gate and marked the majority of CAFs (Fig. 5h). Altogether, we find that
344 LRRC15⁺ TGFB cluster 0 (hC0) CAFs are the most prominent fibroblast population in
345 multiple human PDAC data sets confirming our findings from the mouse model.

346 While human fibroblast clusters 0 and 2 (hC0 and hC2) exhibited overlapping
347 genes of mouse TGFB c2 and IL1 c8 CAFs in a cross-species comparison, respectively
348 (Fig. 5i), cluster 1 (hC1) did not obviously match the early CAF populations observed in
349 mouse. Although HC1 was characterized by high levels of mouse c4 relative to c3
350 genes (Suppl. Fig. 5c), individual cells did not show a clear phenotype of one or the
351 other population. To test if, in contrast to mice, human pancreatic fibroblasts are a
352 homogeneous population, we performed *in silico* isolation of single fibroblast cells from
353 11 non-malignant pancreatic tissues, published as part of Peng, J. *et al.*(41).
354 Dimensionality reduction with UMAP and clustering in reduced space revealed a
355 population of 1,407 fibroblasts (*DCN*, *LUM*, Suppl. Fig. 5d, Suppl. Table 7). Sub-
356 clustering of these cells identified two clusters, of which the minor one (<5% of cells)
357 exhibited high levels of *EPCAM* and other epithelial markers and likely represents an
358 artifact of our *in silico* isolation (Suppl. Fig.5e). The other cluster was characterized by
359 strong expression of *C7* and *CFD*. The strong similarity of markers of these non-
360 malignant fibroblasts to hC1 suggested that hC1 have not undergone extensive
361 transcriptional changes relative to non-malignant fibroblasts. This was confirmed by

362 comparing the average expression profile of these two cell types (Pearson correlation:
363 0.97), where only a few genes changed expression (Fig. 5j). Based on this analysis we
364 were able to identify genes enriched in non-malignant fibroblasts and hC1 CAFs, but not
365 hC0 TGFB CAFs or hC2 IL1 CAFs, as well as genes that are induced in all three CAF
366 populations compared to non-malignant fibroblasts (Suppl. Fig. 5f). Together, the results
367 suggested that hC1 CAFs are early CAFs (eCAF) and the predecessor to both hC2 IL1
368 and hC0 TGFB CAFs. To test this hypothesis, we performed principal component
369 analysis of all fibroblasts including those from non-malignant pancreas. Strikingly, PC1
370 separated cells in the order of non-malignant fibroblasts, hC1 eCAF, hC2 IL1 CAFs and
371 hC0 TGFB CAFs (Fig. 5k). The minimum spanning tree fit to this dimensionality reduced
372 data supported that starting from non-malignant fibroblasts cells undergo a
373 transformation into C1 eCAF, upregulating type 1 collagen, SPARC, and other
374 extracellular matrix proteins. From this intermediate state cells either become hC2 IL1
375 CAFs or hC0 TGFB CAFs. Interestingly, both the hC1 eCAF and the hC0 TGFB CAFs
376 make up almost all fibroblasts in the single-cell dataset under investigation. We did not
377 see evidence of any cells with a mesothelial or apCAF signature in these data, however
378 we find that all human CAFs expressed *CD74* and *HLA-DRA* (Suppl. Fig. 5g), which is
379 consistent with data found in Elyada, et al(36). We have summarized our findings in
380 both human and mouse in a model (Fig. 5l).

381

382 ***A LRRC15⁺ CAF signature can be found across several human cancer indications***

383 As it had been previously reported that stromal LRRC15 expression could be
384 observed in several tumor types(38) we performed a pan-cancer analysis across tumors
385 in The Cancer Genome Atlas (TCGA, n=9,736) and compared these data to matched
386 non-malignant tissues from the GTEx database (n=8,587). We found that *LRRC15*
387 expression was consistently low/absent across normal tissues, but upregulated in a
388 variety of tumors including but not limited to pancreatic, breast, and head and neck
389 cancers (Fig. 6a). To verify that the *LRRC15* signal was derived from TGFB-activated
390 CAFs in tumor types other than PDAC, we first identified a more robust expression
391 signature of TGFB CAFs from our human PDAC scRNA-seq analysis. We focused on
392 genes significantly enriched in TGFB CAFs compared to all other fibroblast populations

393 that showed no/low expression by any other cell type in the full dataset (Fig. 6b). The
394 gene set was strongly enriched in microdissected PDAC bulk stroma vs tumor samples
395 (Fig. 6c), suggesting that their combined signal allows conclusions about the
396 presence/absence of TGFB fibroblasts in bulk RNA-seq data.

397 To next confirm the presence of this population in other tumor types, we
398 exemplarily re-analyzed single-cell RNA-seq data from 18 head and neck squamous
399 cell carcinoma (HNSC) patients(43). Dimensionality reduction with UMAP of 3,363 cells
400 from the TME free of somatic mutations confirmed the cell-type annotations provided by
401 the authors (Fig. 6d, top). Clustering of the mesenchymal cells revealed 5 sub-clusters,
402 of which two were pericytes (25% of all cells, *PDGFRB*, *MCAM*, *RGS5*, *ACTA2*), two
403 were fibroblasts (15% of all cells, *LUM*, *DCN*) and one was myoblastic-like (2% of all
404 cells). Confirming the results from the pancreatic cancer single-cell data, expression of
405 our TGFB CAF marker gene set was almost entirely restricted to one of the two
406 fibroblast clusters (Fig. 6d, bottom right; cluster 2, 60% of all fibroblasts). This
407 underscores the presence of LRRC15⁺ TGFB CAFs also in head and neck cancer.
408 Furthermore, the majority of genes showed low/no expression by tumor cells (Suppl.
409 Fig. 6a), indicating that the main signal of these genes in bulk RNA-seq data is, as we
410 have shown in pancreatic cancer, likely primarily derived from TGFB CAFs and less so
411 from EMT tumor cells.

412 Based on these results we used an 11 gene signature (*MMP11*, *COL11A1*,
413 *C1QTNF3*, *CTHRC1*, *COL12A1*, *COL10A1*, *COL5A2*, *THBS2*, *AEBP1*, *LRRC15*,
414 *ITGA11*) to infer the presence of TGFB CAFs across different cancer types from bulk
415 RNA-seq TCGA data. In this pan-cancer analysis comprising 31 different cancer types
416 from TCGA we found a positive correlation between the average expression and the
417 average gene-wise correlation of our core signature across cancer types (Fig. 6e). The
418 positive correlation indicates that in cancer types where the TGFB CAF is present (high
419 average expression), there is a true signal in the bulk coming from this population that
420 leads to a high gene-wise correlation. In cancer types lacking TGFB CAFs (low average
421 expression) there is just a “noise” signal and the genes are uncorrelated. The analysis
422 points, besides PAAD, to TGFB CAFs playing a strong role also in breast cancer
423 (BRCA), lung cancer (LUSC, LUAD), ovarian cancer (OV), colon cancer (COAD), renal

424 cancer (READ), esophageal cancer (ESCA), Stomach Adenocarcinoma (STAD),
425 bladder cancer (BLCA, [Suppl. Fig. 6b]) as well as head and neck cancer (HNSC). In
426 summary these data suggest that LRRC15⁺ CAFs are a prominent population across
427 multiple human cancer types that emerges from a LRRC15⁻ fibroblast population.

428

429 ***A LRRC15⁺ CAF signature predicts poor clinical response to checkpoint blockade***

430 Having shown that *Lrrc15*⁺ CAFs are present in human cancers, we next sought
431 to test the clinical impact of this population. Due to the known roles of TGFB in
432 modulating immunotherapy(32,44) we evaluated the clinical significance of the newly
433 identified LRRC15⁺ CAF in response to cancer immunotherapy. Multiple reports have
434 shown that the molecular makeup of bladder cancer is similar to pancreatic cancer with
435 shared subtypes(45,46). Further, we have shown in our previous analysis that LRRC15⁺
436 CAFs are a frequent population also in bladder cancer (Fig. 6e). We found that the
437 markers for LRRC15⁺ CAFs identified in PDAC were also significantly co-expressed in
438 RNA-seq data from our recent bladder cancer immunotherapy trial (32) (Suppl. Fig. 7a).
439 Moreover, the signature was associated with worse outcome for patients receiving anti-
440 PD-L1 (Atezolizumab) therapy (p=0.03, HR= 1.4, Suppl. Fig. 7b). This effect is
441 explained by the increased expression of the signature in patients that fail to respond to
442 anti-PD-L1 therapy exclusively in immune excluded tumors, but not in tumors with
443 inflamed or desert immune phenotype (Fig. 7a). Consequently, we observe a significant
444 association of the LRRC15⁺ CAF signature with worse outcome specifically in patients
445 with immune excluded tumors (p<0.001, HR=2.3, Fig. 7b). Our result represents an
446 improvement over the fibroblast TGFB response signature obtained through *in vitro*
447 activation of fibroblasts with TGFB in regards to their cell-type specificity (Fig. 7c) and
448 predictive power (Fig. 7d). Immunoscoring of PDAC patients revealed the majority
449 showed an immune excluded phenotype, suggesting these findings might also apply to
450 PDAC patients (Suppl. Fig 7c). Importantly, the LRRC15⁺ CAF signature was also
451 predictive of response to Atezolizumab in a second trial comprising multiple other
452 cancer types, such as renal cell carcinoma, head and neck cancer, and non-small cell
453 lung cancer (Fig. 7e, Suppl. Fig. 7d, p=0.01, HR=2.01). This effect (HR>1.5) was
454 apparent across several individual cancer indications, despite their small individual

455 sample sizes (Suppl. Fig 7e). It remains unclear what the nature of LRRC15⁺ CAF
456 immunosuppression might be, but these data provide a strong basis to further elucidate
457 the functions of these cells. The correlation between LRRC15⁺ CAFs and poor outcome
458 in immunotherapy treatment suggests that multiple tumor indications may benefit from
459 LRRC15 CAF reprogramming combined with immunotherapy.

460

461 **DISCUSSION**

462 Here, we took advantage of our novel digestion method to profile PDPN⁺ CAFs
463 *ex vivo* using scRNA-seq. Our approach identified two separate populations of normal
464 tissue fibroblasts(ntFib) in mouse pancreas. Their expression signatures suggest
465 disparate functions, with one more primed to provide structural support and another
466 appearing more immunoregulatory. These two separate lineages evolve separately into
467 IL1- and a TGFB- driven CAFs in the context of PDAC. Further work on localization and
468 lineage tracking will allow us to distinguish whether there is a physical
469 compartmentalization or niche that results in differential exposure to IL1 and TGFB or
470 whether the ntFibs fundamentally have differing potential to respond to IL1 and TGFB
471 that results in the two separate CAF trajectories we observe.

472 Our findings from murine late-stage tumors support previous observations
473 identifying IL1 driven “iCAF” and TGFB driven “myCAFs”(40,47). Furthermore, we
474 provide new insights into how resting fibroblast heterogeneity pre-determines the fate of
475 stromal cells in the TME. It also seems from our cross comparison that “iCAFs” include
476 both our early CAF1 and IL1 CAF while “myCAFs” include both our early CAF2 and
477 TGFB CAF. We do observe a difference with our identification of a population previously
478 designated as an “apCAF”(36), that we identify a mesothelial cell population. This
479 discrepancy might be due to mesothelial cells acquiring some fibroblasts genes in the
480 KPC system as mesothelial to mesenchymal transition has been described in some
481 tissues(48). In fact, in the KPC system a relationship between the “apCAF” and
482 “myCAF” is apparent in UMAP space and the “apCAFs” express *Pdgfra* suggesting
483 changes from the normal tissue state. However, the dominant mesothelial genes driving
484 the clustering of that population, including the antigen presenting genes *CD74* and *H2-*
485 *Ab1*, were present in normal pancreas. We also did not observe these cells in the

486 tumor, which may be a consequence of our dissection method where the majority of the
487 mesothelium would be included in the adjacent normal tissue or it could reflect a
488 difference between the KPC and KPP models.

489 Comparison to several different human patient cohorts revealed both similarities
490 and differences with the mouse which we have modelled (Fig. 5I). While the
491 conservation of IL1 and TGFB CAFs was quite obvious, we were struck by several
492 differences between the mouse models and human patient data. First, we do not
493 observe baseline heterogeneity in the human non-malignant tissue fibroblasts. Rather
494 human fibroblasts from non-malignant tissue show a transcriptional profile that
495 combines the mouse ntFIB signatures. Subsequently, non-malignant human fibroblasts
496 transition to a single early CAF which then gives rise to either a TGFB or IL1
497 programmed CAF. However, given the human tissues we analyzed were not truly
498 normal we cannot rule out that non-malignant fibroblasts had already undergone
499 changes that masked baseline heterogeneity. We also find that *CD74* and *HLA-DRA*
500 are expressed by all human CAF populations, revealing a potentially important
501 functional difference between human and mouse CAFs. We do not observe a specific
502 population with a similar transcriptional signature to “apCAF” or mesothelial cells
503 suggesting this population is absent or very rare in the TME of PDAC.

504 We identify the TGFB-driven cell population as the most prevalent CAF in late-
505 stage tumors, and show that surface expression of LRRC15 enables experimental
506 isolation and manipulation of these CAFs both in mouse models and human patient
507 samples. Furthermore, we find that the LRRC15⁺ CAF signature correlates with poor
508 response to checkpoint blockade in several different human tumors. These cells have
509 myofibroblastic properties and a dominant ECM gene signature. We find they constitute
510 the majority of CAFs in PDAC patients, which are dominantly of an immune excluded
511 phenotype. This suggests an immunoregulatory role for these cells. It will be valuable to
512 further explore whether early CAFs can be prevented from adopting the pro-tumorigenic
513 fate of the LRRC15⁺ CAF or whether the LRRC15⁺ CAF phenotype can be reverted to
514 improve immunotherapy efficacy.

515 While we chose to focus on the LRRC15⁺ CAFs, due to their prevalence in
516 PDAC, IL1 CAFs have a transcriptional program clearly suggesting immune regulation

517 of the TME. Inhibition of Jak signaling in PDAC has shown both a reduction in IL1 CAFs
518 and reduced tumor burden(47), although it is difficult to distinguish direct effects of
519 these inhibitors on the tumor cells(28,49–51) from the effects of IL1 CAF loss in the
520 TME. It is also important to note that while both of these CAFs have many
521 transcriptional differences they also both express genes associated with myofibroblast
522 characteristics and both express various immune regulatory and even inflammatory
523 mediators. Thus, we describe them by their most conserved characteristics, their major
524 transcriptional programming; IL1 CAF and TGFB CAF. For the TGFB CAF we have
525 identified LRRC15 expression as a good proxy across several cancer indications.

526 We chose to focus on fibroblasts to generate a robust data set that would be a
527 good representation of the heterogeneity of a somewhat rare population. Our work also
528 identifies other populations with fibroblast properties: PDPN⁻ CD31⁻ cells which were
529 enriched for pericytes, but adopted expression of some CAF genes, as well as two
530 populations of PDPN⁺ cells, which we classified as tumors cells undergoing EMT. There
531 are also various stromal and non-stromal cells that we chose to leave out of the focus
532 this study. These cells are all part of the TME and future research into their functions is
533 sure to yield a more complete understanding of their interactions and contributions to
534 tumor progression and response to therapy.

535

536

537

538 **METHODS**

539 ***Mice***

540 WT B57BL/6 mice (colony 000664) and albino WT B6(Cg)-Tyrc-2J/J mice (colony
541 000058), mice were purchased from Jackson. We licensed Kras^{LSL.G12D} from Tyler
542 Jacks (Massachusetts Institute of Technology, Boston), p16/p19^{fl/fl} from Anton Berns
543 (NKI, Amsterdam), and Pdx1.Cre from Andy Lowy (University of Ohio). Pdx1^{cre/+};LSL-
544 Kras^{G12D/+};p16/p19^{flox/flox} (KPP) mice were generated as previously described(12).
545 Age- and sex-matched mice were used for experiments. The mice were housed at
546 Genentech in standard rodent micro-isolator cages and were acclimated to study
547 conditions for at least 3 days before tumor cell implantation. Animals were 6-12 weeks
548 old.

549 KPP GEMM mice were euthanized at median ages of 9 wk. This age reflects the
550 disease state with high penetrance adenocarcinoma and at which the GEMMs with
551 moderate and large tumors are observed.

552 All animals were monitored according to the guidelines from the Institutional Animal
553 Care and Use Committee (IACUC) at Genentech, Inc.

555 ***Cell lines***

556 The KPP14388 murine pancreatic adenocarcinoma cell line was generated by the
557 Junttila group at Genentech from the KPP GEMMs. Transgenic lines were created as
558 follows: mApple MSCV retrovirus was transfected into KPP14388 and a single clone
559 was grown out; KPP-DTR was obtained by transducing KPP-14388 with DTR-efp
560 lentivirus and single-cell clone was selected. Cancer cells were cultured in High
561 Glucose Dulbecco's Modified Eagle Medium (DMEM) medium plus 2 mM L-glutamine
562 with 10% fetal bovine serum (FBS; HyClone, Waltham, MA). All cell lines were tested
563 for mycoplasma by qPCR. For all injected tumors cells were used within the first three
564 passages.

566 ***Tissue digestion, cell isolation and flow cytometry of murine tissues***

567 To isolate pancreases, first the omentum was removed then the pancreas collected with
568 careful exclusion of draining lymph nodes. The pancreas was then minced. For stellate

569 cell enrichment tissue was digested as previously described(11). Enzymatic digestion
570 was used with 0.02% Pronase (Roche cat 10165921001), 0.05% Collagenase P
571 (Roche, cat. 11249002001), and 0.1% DNase (Roche, cat. 10104159001) in Gey's
572 balanced salt solution (Sigma cat G9779) for 50 min. Digested tissue was then filtered
573 through a 100- μ m nylon mesh. Cells were centrifuged at 1300rpm for 5min, washed and
574 then resuspended in GBSS containing 0.3% bovine serum albumin (Sigma Aldrich cat
575 A2153). The cell suspension was centrifuged, decanted and resuspended into 8ml
576 28.7% (wt/vol) solution of Nycodenz (Sigma, no longer available. Also used 16.7%
577 Optiprep[Sigma-Aldrich D1556]) overlaid with 6ml .3% BSA GBSS, then centrifuged at
578 1400g with no break for 20 min. The cells of interest separated into a fuzzy band just
579 above the interface of the Nycodenz cushion and the GBSS. This band was harvested,
580 and the cells were washed and resuspended in MACs buffer.

581 For our new digest, which was modified from Fletcher, et al.(52), 20 μ g/ml anti-
582 trypsin (Sigma Aldrich cat 10109886001) was used in first round of digest incubations
583 which were prepared as follows. Pancreases were enzymatically digested using
584 800 μ g/ml Dispase), 400 μ g/ml collagenase P, and 100 μ g/ml DNaseI at 37°C. Fractions
585 were collected into Macs buffer and digest media was refreshed 2 more times after
586 15min, 10min, and 5 min incubations. At this point either: 1) for comparison to stellate
587 cell enrichment the cell suspension was centrifuged at 1300rpm for 5min, decanted,
588 subjected to a density gradient as described above. 2) For subsequent digests without
589 gradient enrichment, samples underwent RBC lysis and were spun for 4 min at 50g to
590 pellet debris, supernatant was collected, spun down and resuspended in media and
591 cells were counted using a Vi-CELL XR (Beckman Coulter, Brea, CA).

592 Pancreatic tumors were similarly treated with the addition of 2U/ml hyaluronidase
593 (Worthington cat LS002592) and 20U/ml purified collagenase (Worthington LS005273)
594 and 100 μ g/ml CollagenaseP. In PDAC experiments control normal pancreases were
595 digested using same enzymatic cocktail as tumors. Tumors also often required 1-2
596 additional digest incubations to break down tissue.

597 Subcutaneous tumors were collected with care to avoid draining lymph node and
598 epidermis. Subcutaneous tumors were weighed and enzymatically digested using the

599 same enzymatic mix as the previously described normal pancreas samples, without the
600 trypsin inhibitor addition.

601 Cells were labeled with mAbs purchased from eBioscience, BioLegend, or BD
602 Biosciences at 1:200 for 20-30 min, unless otherwise noted. Prior to cell surface
603 staining with the following fluorescently labeled antibodies, cells were blocked with Fc
604 block (2.4G2; 1:500). Surface staining for experiments was performed using antibodies
605 described in [Suppl. Table 8](#) for 25min at 4c, washed 2.5 times with MACs buffer, then
606 either fixed (Biolegend cat 420801) or resuspended in 7AAD (1:50; BD cat 559925) and
607 Calcein Blue(1:1000; Invitrogen, cat. C1429) for cytometry analysis. For intracellular
608 staining, cells were surface stained as above, washed, and then fixed and
609 permeabilized using the FoxP3 ICS kit (eBiosciences cat 00-5523-00), per the
610 manufacturer's directions. Cells were then incubated with antibodies described in [Suppl.](#)
611 [Table 8](#) for 1 hour in perm buffer. Data were acquired on a Fortessa, Symphony or
612 LSRII (BD Biosciences) and analyzed using FlowJo (Tree Star).

613

614 ***Aldefluor assay***

615 Cells were isolated as above. Once a single-cell suspension was obtained, cells were
616 plated and resuspended in aldefluor assay buffer, as part of the aldefluor kit
617 (STEMCELL, cat. 01700) in FACS tubes (500uL) or 96 well U bottom plates (200uL)
618 with Fc block. Then, 10uL (FACS tubes) or 4uL (96 well plate) of assay buffer was
619 aliquoted into quench tubes. 2.5uL (FACS tubes) or 1uL (96 well plates) of DEAB buffer
620 was aliquoted into quench tubes. 5uL (FACS tubes) or 2uL (96 well plate) aldefluor
621 reagent was then added to cells as rapidly as possible. Cells were then mixed and ½ of
622 the volume was added to quench tubes with DEAB. Samples were incubated at 37C for
623 15-20 minutes, then spun down and surfaced stained as above on ice for 20-30 minutes
624 before FACS analysis.

625

626 ***Anti-LRRC15 antibodies for flow cytometry and murine imaging***

627 Gene synthesis and cloning was performed following reverse translation and codon
628 optimization for Chinese hamster ovary (CHO) cells of the amino acid sequences
629 encoding the variable heavy (VH) and variable light (VL) domains of huM25 (flow) and

630 huAD208.4.1 (imaging) anti-LRRC15 clones, as published via patent 10195209(53). For
631 huM25, expression constructs of human-mouse chimeric antibodies were generated by
632 subcloning the VL and VH sequences into mammalian expression vectors containing
633 mouse kappa light chain and mouse IgG2a heavy chain frameworks, respectively. For
634 huAD208.4.1, expression constructs of human antibodies were generated by subcloning
635 the VL and VH sequences into mammalian expression vectors containing human kappa
636 light chain and human IgG1 heavy chain frameworks, respectively. Both antibodies
637 were produced by transiently-transfected CHO cells and purified using standard
638 antibody purification methods and were confirmed to be human/mouse LRRC15 cross-
639 reactive by surface plasmon resonance (data not shown).

640

641 ***Immunofluorescence and image analysis of mouse tissues***

642 Mouse pancreas, PDAC tumor tissue, and subcutaneous KPP and KPR tumors were
643 fixed overnight in 1% PFA, embedded in optimal cutting temperature medium (Sakura
644 Finetek) and frozen for storage at -80C. 5-12 microns thick sections were
645 cryosectioned, immune-stained, and imaged with confocal microscope Leica TCS SP8.
646 Images were processed with Fiji [software](#) (ImageJ v2.0.0-rc-69/1.52i). For staining
647 slides were fixed for 5min in 4%PFA, blocked and permeabilized in stain buffer(2% BSA
648 5%Goat Serum in PBS) with .3%triton for 1 hour. Primary antibodies were added for 1hr
649 RT to overnight at 4C, secondaries were added for 30m-2hours at RT slides were
650 mounted in hardening media (Dako S3023). Details of the antibodies used can be found
651 in [Suppl. Table 8](#).

652

653 ***Tumor implantation***

654 Cells between passage 1-2 were trypsinized, filtered, counted, and resuspended in 50%
655 PBS and 50% Matrigel (Corning cat 356231) at a concentration of 1×10^6 cells/mL for
656 injection into mice. The mice were housed at Genentech in standard rodent micro-
657 isolator cages and were acclimated to study conditions for at least 3 days before tumor
658 cell implantation. Animals were 6-10 weeks old. Only animals that appeared to be
659 healthy and free of obvious abnormalities were used for studies. Mice were inoculated
660 in the right flank with 1×10^5 cancer cells in 100 μ L of PBS:Matrigel (1:1). 16-24 days

661 after tumor injection, mice were euthanized and tumors collected for either IF or flow
662 cytometry analysis.

663

664 ***Spheroid cultures***

665 Donor B6 mice were injected with KPP-DTR cancer cells as described above. Tumors
666 were collected and digested. Single-cell suspensions were spun down at 1300RPM for
667 3min, decanted, and resuspended in fibroblast media (10% FBS α MEM, supplemented
668 1x L-Glutamine, 1x Pen/Strep, and 1x HEPES (all from Gibco) and 10% batch tested
669 low IgG Fcs (Gemini)). Bead depletion was performed with anti-cd45-bio, anti-cd24-bio,
670 and anti-cd31-bio in conjunction with the Easy-sep Biotin selection kit(STEMCELL cat
671 17655)). Cells were then sorted for LRRC15+ CAFs and LRRC15- Ly6C+ CAFs, as
672 controls normal pancreas was sorted for ENG+LY6c- and ENG-LY6C+ fibroblasts as
673 described in flow cytometry panels. Sorted cells were cultured in fibroblast media, 25ng
674 of Diphtheria Toxin (DT, Enzo cat BML-G135-0001) was added to kill Tumor cells, this
675 was done in 100mm tissue culture treated dishes with 20ml media. Plates were rinsed
676 the next day with PBS and media with DT was replaced. Cells were cultured for 7-10
677 days week, with one passage at confluence, to expand fibroblasts. Cultured fibroblast
678 cells were trypsinized counted, then combined with KPP-mApple cancer cells.

679 For spheroids, 2000 KPP-mApple cancer cells were seeded in 100ul matrigel
680 (Corning cat 356231) with or without different fibroblasts populations(15k). Before
681 plating cells, 100ul of Matrigel was spread on each well of a 24-well glass-bottom
682 plate(Mattek) and allowed to polymerize, to keep cells from directly colonizing glass. 2
683 mls of fibroblast media was added to each well. The plate was imaged 2-4 times a week
684 with a 4x Plan Fluor objective (NA: 0.13, Nikon) on a Nikon Ti-E inverted microscope
685 equipped with a Neo scMOS camera (Andor, Oxford Instruments), a linear encoded
686 automated stage (Applied Scientific Instrumentation), 37C/5% CO2 environmental
687 chamber (Okolab), all run by NIS Elements software (Nikon). Image sets in TRITC and
688 brightfield of the Matrigel bubble were stitched and focused into one image projection
689 with an extended depth of focus module (EDF, Nikon). The resulting TRITC EDF image
690 was analyzed in Matlab (vR2018a, Mathworks) to measure total mApple spheroid area.

691

692 ***Tissue digestion, cell isolation and flow cytometry of human tissues***

693 Human PDAC tumor samples were obtained and digested using a previous published
694 protocol(9). PDAC samples were fragmented into small pieces (around 1mm³) and
695 digested in CO₂-independent medium (Gibco, cat18045-054) supplemented with 5%
696 fetal bovine serum (FBS, PAA, catA11-151), 2 mg/ml collagenase I (Sigma-Aldrich,
697 catC0130), 2 mg/ml hyaluronidase (Sigma-Aldrich, catH3506) and 25 mg/ml DNase I
698 (Roche, cat11284932001) for 45 min at 37C with shaking (180-200rpm). After tissue
699 digestion, cells were filtered using a cell strainer (40 mm, Fisher Scientific,
700 cat223635447) and resuspended in PBS+ solution supplemented with 2 mM EDTA and
701 1% Human serum (Sigma P2918) to a final concentration at approximately 5x10⁵ cells
702 in 50 ul. Tissue single cell suspension was stained with antibody cocktail described in
703 [Suppl.Table 8](#).

704

705 ***Immunohistochemistry and image analysis of human tissues***

706 Tissues were fixed in 10% neutral Buffered formalin for 24 hours, then dehydrated and
707 paraffin embedded, and sectioned into 4um slices. Slides were de-paraffinized and
708 antigen retrieved in CC1 buffer (TRIS-EDTA pH 8.1) at 95C for 64min. Sequential
709 staining with elution step after first antibody detection was completed. First antibody
710 anti-LRRC15 Abcam ab150376 used at 2.5ug/ml. Elution was done with CC2 buffer
711 (Citrate-Acetate based with SDS 0.3% (pH 6.0)) Time: 8 min @ 100C. Second antibody
712 was anti-cd8 Abcam ab101500 used at 1:200 and the isotype control for both was
713 Naïve rabbit monoclonal CST cat 3900S. The detection system used was OmniMap-
714 Rbt-HRP with DAB for CD8 and OmniMap-Rbt-HRP with Discovery purple for LRRC15.

715 Patient slides were immunoscored by pathologist with expertise in the field, H.K.
716 Bright field images were acquired by a Hamamatsu Nanozoomer automated slide-
717 scanning platform at a final magnification of 200x. The images were analyzed with the
718 2019a version of the Matlab software package (MathWorks). LRRC15⁺ fibroblasts and
719 CD8 cell nuclei were segmented by intensity thresholding and simple morphological
720 filtering of the image.

721

722 ***Generation of bulk-sorted RNA sequencing***

723 Single-cell suspensions were isolated as described above. For sorting described in
724 Figure1; 4 individual animals/group were sorted from the following: healthy albino B6
725 pancreas, KPP pancreas bearing tumors <4mm, or KPP pancreas with tumors > 10mm.
726 Samples were stained and sorted for EPCAM-, CD45-, TER119-, ITGA6-, CD31-, viable
727 (life Technologies) and then PDPN+ PDGFRa+ or PDPN- populations where sorted
728 directly into trizol, purity was assessed on a small aliquot sorted into PBS as 95% or
729 higher. RNA was isolated according to Universal RNeasy kit (Qiagen). RNA was profiled
730 with the Bioanalyzer Pico RNA Kit (Agilent Technologies). Low-input RNA kit (Clontech)
731 was used to generate cDNA libraries. RNA-seq libraries were multiplexed and
732 sequenced using HiSeq4000 to generated 30 M single end 50 bp reads per library.

733

734 ***Generation of Single-Cell sequencing libraries***

735 For single-cell sequencing. Albino B6 and KPP age and sex matched mice animals
736 were sacrificed, for each of 2 replicates; 5 albino B6 pancreases where used for
737 “normal”, 5 KPP animals where used for other samples with tissues being divided into
738 “adjacent” (no masses), “small tumors” (tumors <4mm), and “large tumors” (tumors
739 5mm-10mm). Single-cell suspensions were isolated as described above. Samples were
740 stained and sorted for CD45-, TER119-, CD24a-, CD31-, 7AAD-, Calcein Violet+,
741 PDPN+. Sorted single-cell suspensions were converted to barcoded scRNA-seq
742 libraries by using the Chromium Single Cell 3' Library, Gel Bead & Multiplex Kit and
743 Chip Kit (10x Genomics), loading an estimated 6,000 cells per library and following the
744 manufacturer's instructions. Samples were processed using kits pertaining to either the
745 V2 barcoding chemistry of 10x Genomics. Single samples were processed in a single
746 well of a PCR plate, allowing all cells from a sample to be treated with the same master
747 mix and in the same reaction vessel. For each replicate, all samples (non-malignant and
748 tumor) were processed in parallel in the same thermal cycler. The final libraries were
749 profiled using the Bioanalyzer High Sensitivity DNA Kit (Agilent Technologies) and
750 quantified using the Kapa Library Quantification Kit (Kapa Biosystems). Each single-cell
751 RNA-seq library was sequenced twice in two lanes of HiSeq4000 (Illumina) to obtain
752 single end, 98 bp, ~500M reads per library.

753

754 **Bioinformatic processing of mouse scRNA-seq data**

755 Single-cell RNA-seq data for each replicate were processed with cellranger count
756 (CellRanger 2.1.0 [10x Genomics]) using a custom reference package based on mouse
757 reference genome GRCm38 and GENCODE gene models. Individual count tables were
758 merged using cellranger aggr to reduce batch effects. Subsequent data analysis was
759 carried out in R 3.5.1 and the Seurat package (v 2.3.4). From an initial set of 14,916
760 cells, counts of transcripts measured as unique molecular identifiers (UMIs) in each cell
761 were normalized and log transformed to $\log(\text{CPM}/100+1)$ [CPM=UMI counts per
762 million]. Cells with at least 1,200 measured genes per cell were considered for analysis.
763 To remove noise from droplets containing more than one cell, we focused on cells with
764 at most 5,000 measured genes. Dead cells were excluded by retaining cells with less
765 than 3% mitochondrial reads leaving 13,454 cells for final analysis. Genes induced due
766 to dissociation stress of single cells published previously(54) were used to score the
767 dissociation stress in each cell with the *AddModuleScore* function in Seurat (see section
768 Calculation of single cell scores for details). Subsequently, normalized data was scaled
769 to regress out the number of distinct UMIs and the stress signature score.

770 Prior to dimensionality reduction we performed batch correction with Harmony
771 (55) version 0.0.0.9000 as described in the tutorial at
772 [http://htmlpreview.github.io/?https://github.com/immunogenomics/harmony/blob/master/](http://htmlpreview.github.io/?https://github.com/immunogenomics/harmony/blob/master/docs/SeuratV2.html)
773 [docs/SeuratV2.html](http://htmlpreview.github.io/?https://github.com/immunogenomics/harmony/blob/master/docs/SeuratV2.html) We adjusted the cluster membership penalty parameter to theta to
774 1, in order to put a less strong force on combining cells across replicates.
775 Dimensionality reduction was carried out with the Seurat package(56). Prior to principal
776 component analysis we identified the 1,000 most variable genes (Seurat,
777 *FindVariableGenes* using the mean of logged values and the variance to mean ratio
778 (VMR) in non-logspace) and applied PCA to cells in this gene space. Principal
779 components 1 to 20 were provided as an input for dimensionality reduction via tSNE
780 and UMAP with default parameters in Seurat. Clusters of cells were identified based on
781 a shared-nearest neighbor graph between cells and the smart moving (SLM) algorithm
782 (k=40, resolution = 0.7). Markers for each cluster were identified by reducing the
783 number of candidate genes to those genes which were a) at least $\log(0.25)$ fold higher
784 expressed in the cluster under consideration compared to all other clusters and b)

785 expressed in at least 10% of cells in the cluster under consideration. For genes passing
786 those criteria significance between cells in the cluster vs all other cells was calculated
787 using Wilcoxon's rank sum test and adjusted with the Benjamini Hochberg method.

788

789 ***Calculation of single-cell scores***

790 Scores for single-cells were calculated as the average relative expression of a gene set
791 of interest, minus the average relative expression of a control gene set to account for
792 technical differences between cells, as described by Tirosh et al. (57) and implemented
793 in the Seurat AddModuleScore function. To obtain the geneset for lineages P3 and P4,
794 we used the 20 most significantly upregulated (adj. p-val. <0.00001, sorted by average
795 logFC) genes in each of the two normal populations to score all cells for these two
796 expression programs. To obtain a Collagen signature, we used all Collagen encoding
797 genes expressed in the full dataset to score each cell.

798

799 ***Pseudotime reconstruction***

800 Single-cell pseudotime trajectories were constructed with Monocle version 2.8.0
801 independent for each of the two fibroblast lineages, as Monocle 2 does not support
802 trajectories with multiple roots. For each trajectory we collected a set of 400 ordering
803 genes that defined CAF progression by testing each gene for differential expression
804 between normal fibroblasts from the respective lineage and fibroblasts from late-stage
805 tumors (adj. p<0.001, sorted by logFC, 200 most up and 200 down regulated genes).
806 Expression profiles were reduced to two dimensions using the DDRTree algorithm
807 included with Monocle 2 via the reduceDimension method and cells ordered along the
808 trajectory using the orderCells method, both with default parameters.

809

810 ***Enrichment analysis***

811 Pathway and Gene Ontology enrichments for cluster-specific genes were calculated
812 using ConsensusPathDB(58) and DAVID(59), respectively. Genes with an adj. p
813 <0.00001, log(0.25) fold higher expressed in the cluster, and expressed in >10% of cells
814 served as an input for analysis. Transcription factor binding site (TFBS) enrichment was
815 calculated using the OPOSSUM web service(60). Pathways with adjusted p-value <0.05

816 were considered significantly enriched for pathway analysis, TF motifs with a z-score
817 >10 were considered enriched. The z-score calculation in OPOSSUM uses the normal
818 approximation to the binomial distribution to compare the rate of occurrence of a TFBS
819 in the target set of genes to the expected rate estimated from a pre-computed
820 background set.

821

822 ***Bioinformatic processing of bulk RNA-seq data***

823 Bulk RNA-seq data from GEMM and subcutaneous mouse models was processed as
824 described previously (32). Briefly, reads were aligned to the mouse reference genome
825 (mm10) using GSNAP version '2013-10-10', allowing a maximum of two mismatches
826 per 75 base sequence (parameters: '-M 2 -n 10 -B 2 -i 1 -N 1 -w 200000 -E 1 --pairmax-
827 rna=200000 --clip-overlap'). To quantify gene expression levels, the number of reads
828 mapped to the exons of each gene was calculated in a strand-specific manner using the
829 functionality provided by the R package GenomicAlignments. For heatmap
830 visualizations, per-gene counts were normalized to Reads Per Kilobase Million (RPKM)
831 within each sample to account for differences in transcript length and sequencing depth.

832 Differentially expressed genes between groups were determined using the R
833 package limma (61) after trimmed mean of M-values (TMM) normalization, which
834 implements an empirical Bayesian approach to estimate gene expression changes
835 using moderated t-tests.

836

837 ***Bioinformatic processing of human PDAC scRNA-seq data***

838 Data from 24 PDAC patients and 11 control pancreas tissues was obtained from the
839 Genome Sequence Archive under project PRJCA001063 in FASTQ format. Single-cell
840 RNA-seq data for each patient was processed with cellranger *count* (Cell Ranger 3.0.2
841 [10x Genomics]) using standard parameters and supplying a custom reference package
842 based on human reference genome GRCh38 and GENCODE gene models. Samples of
843 22 patients and 11 control tissues for which the correct chemistry was detected by Cell
844 Ranger from the sequencing data were used for downstream analysis.

845 Subsequent data analysis was carried out in R 3.5.1 and the Seurat package (v
846 3.0.2). Cells with at least 300 measured genes per cell were considered for analysis. To

847 remove noise from droplets containing more than one cell, we focused on cells with at
848 most 6,000 measured genes. Dead cells were excluded by retaining cells with less than
849 15% mitochondrial reads leaving 84,276 cells for final analysis. Subsequently, data was
850 normalized to $\log(\text{CPM}/100+1)$ and scaled regressing out the number of distinct UMIs
851 and the fraction of mitochondrial reads during scaling.

852 Dimensionality reduction was carried out with the Seurat package. Prior to
853 principal component analysis we identified the 2,000 most variable genes and applied
854 PCA to cells in this gene space. Principal components 1 to 20 were provided as an input
855 for dimensionality reduction via UMAP with default parameters. Clusters of cells were
856 identified based on a shared-nearest neighbor graph between cells and the smart
857 moving (SLM) algorithm (resolution = 0.1). Markers for each cluster were identified by
858 reducing the number of candidate genes to those genes which were a) at least
859 $\log(0.25)$ -fold higher expressed in the cluster under consideration compared to all other
860 clusters and b) expressed in at least 10% of cells in the cluster under consideration. For
861 genes passing those criteria, significance between cells in the cluster vs. all other cells
862 was calculated using Wilcoxon's rank sum test and adjusted with the Benjamini
863 Hochberg method(62). Average expression within individual clusters was calculated
864 with the *AverageExpression* function in Seurat and subsequently z-score transformed
865 for each gene. The minimum spanning to infer global lineage structure of CAFs was
866 calculated using Slingshot(19) with default parameters and defining normal fibroblasts
867 (leftmost population of PC1) as starting and TGFB CAFs (rightmost population of PC1)
868 as end point. KRAS G12X mutations in each cell were manually identified from
869 individual reads in BAM alignment files visualized *via* IGV (63) and assigned to a cell via
870 the CB tag in the BAM file. Copy-number alterations were inferred from single-cell RNA-
871 seq data with the CONICS R package(64) using non-malignant acinar cells as reference
872 cells. The default filtering and normalization procedures were followed, as outlined in
873 <https://goo.gl/tFYLEh>.

874

875 ***Bioinformatic processing of human HNSC scRNA-seq data***

876 Normalized data from 18 HNSC patients(43) was obtained from GEO (GSE103322) as
877 $\log(\text{CPM}/10+1)$ transformed gene-by-cell count matrix. Annotations of cell types

878 (malignant/non-malignant, as well as immune and stromal cell types for non-tumor cells)
879 for each cell were downloaded from the same GEO repository. Data was scaled
880 regressing out the number of distinct UMIs and the different usage of enzymes for
881 scRNA-seq library preparation during scaling. Dimensionality reduction was carried out
882 with the Seurat package. Prior to principal component analysis we identified the 2,000
883 most variable genes and applied PCA to cells in this gene space. Principal components
884 1 to 30 were provided as an input for dimensionality reduction via UMAP with default
885 parameters in Seurat (v3.0.2). Clusters of cells were identified based on a shared-
886 nearest neighbor graph between cells and the smart moving (SLM) algorithm (resolution
887 = 0.4).

888

889 ***Bioinformatic processing of mouse KPC scRNA-seq data***

890 Normalized fibroblast-enriched data from 4 KPC mice(36) was obtained from GEO
891 (GSE129455) as log (number of UMIs in each cell is equal to the median UMI count
892 across the dataset) transformed gene-by-cell count matrix. Ensembl IDs were converted
893 to gene names using the biomart R package(65) Data was scaled regressing out the
894 number of distinct UMIs during scaling. Dimensionality reduction was carried out with
895 the Seurat package. Prior to principal component analysis we identified the 3,000 most
896 variable genes and applied PCA to cells in this gene space. Principal components 1 to
897 20 were provided as an input for dimensionality reduction via UMAP with default
898 parameters in Seurat (v3.0.2). Clusters of cells were identified based on a shared-
899 nearest neighbor graph between cells and the smart moving (SLM) algorithm (resolution
900 = 0.2).

901

902 ***Bioinformatic processing of human bulk RNA-seq data***

903 Comparisons of normalized *LRRC15* levels between tumors from TCGA and their host
904 tissues from GTEx were retrieved from the GEPIA (66) web platform and filtered for
905 tumor types with significant differences between normal and tumor tissue. Raw
906 expression counts per sample of microdissected stroma (n=122) and tumor (n=65)
907 samples(42) were downloaded from GEO (GSE93326). Raw expression counts per
908 sample of normal pancreas RNA-seq (n=247) was downloaded from GTEx (67). Both

909 datasets were normalized to $\text{Log}_2(\text{CPM}+1)$ and heatmaps were generated using the
910 pheatmap R package (<https://cran.r-project.org/web/packages/pheatmap/>) using
911 complete linkage clustering and with Euclidean distance as distance measure.

912 For pan-cancer TCGA data analysis the TCGA Pan-Cancer (PANCAN) batch effects
913 normalized mRNA data was downloaded from the UCSC XenaBrowser
914 (<https://xenabrowser.net>) providing a gene by samples matrix of $\text{log}_2(\text{norm_value}+1)$
915 counts table and patient metadata. From the initial set of $n=11,060$ samples, we only
916 utilized those samples that were annotated as “Primary Tumor” or “Additional - New
917 Primary” in the metadata table resulting in 9,712 samples from 31 different cancer
918 types.

919

920 ***Analysis of Immunotherapy trial data***

921 Whole transcriptome data from patients enrolled in anti PD-L1 (Atezolizumab)
922 immunotherapy trial imvigor 210 (NCT02951767, NCT02108652)(68), were generated
923 as described previously (32). Data from anti PD-L1 (Atezolizumab) immunotherapy trial
924 PCD (NCT01375842) were generated as given in(69). For calculation of LRRC15 CAF
925 scores from expression data, the signature is computed by using the
926 *eigenWeightedMean* method from the MultiGSEA R package
927 (<https://github.com/lianos/multiGSEA>). Briefly, the expression of each gene in a
928 signature is first z-score transformed. Then, a principal component analysis was
929 performed, weights for the genes are calculated by the percent of which they contribute
930 to the first principal component indicated by eigengene. Last, a weighted average per
931 sample is calculated as the final score. This approach has the advantage of focusing
932 the score for the set on the largest block of well-correlated (or anti-correlated) genes in
933 the set, while downweighting contributions from genes that do not track with other set
934 members.

935 For survival analysis, patients were split into low and high expression groups by
936 median. Kaplan-Meier curves were generated using the RMS R package (
937 <http://biostat.mc.vanderbilt.edu/wiki/Main/Rrms>).

938

939 ***Data availability***

940 The single-cell RNA-seq data from mouse PDAC KPP GEMMs are available from the
941 ArrayExpress database (<http://www.ebi.ac.uk/arrayexpress>) under accession number E-
942 MTAB-8483.

943 .

944

945

946 **Acknowledgements**

947 Our flow cytometry core group performed all the cell sorting described in this study. Our
948 in-house genotyping and murine reproductive technology core groups were invaluable
949 for the work done in this study. Thanks to Alex T. Ritter for his advice on the
950 construction of the retroviruses used in this project. Thanks to Jeffrey Eastham-
951 Anderson for his expertise and advice in automated quantification of imaging data.
952 Thanks to members of the Turley laboratory for their scientific input and discussion.

953

954 **Author Contributions**

955 S.J.T and C.X.D designed the experiments within this study. S.J.T, C.X.D, and S.M.
956 wrote the manuscript. C.X.D performed the studies described with contribution on
957 animal immunofluorescence from B.B. and in vivo help from A.C. S.M. performed critical
958 bioinformatic analysis of all sequencing data, both generated for this study or publicly
959 available, with contribution from Y.S. and supervision from C.K. and R.B. S.K. and H.K.
960 performed all staining of human samples and H.K performed scoring of human PDAC
961 patient slide samples. J.H. provided digital pathology expertise. Z.M. and Y.L.
962 performed all sequencing generated in this study. M.J. provided parental cell lines for in
963 vivo tumor injection studies as well as samples and expertise on GEMM models. O.F.
964 provided H&E imaging and expertise on mouse models of PDAC. S.G. provided
965 analysis of spheroid growth. T.W.B. generated the anti-LRRC15 antibodies used in
966 these studies.

967

968

969

970

971

972 **REFERENCES**

- 973
- 974
- 975 1. Stark AP, Sacks GD, Rochefort MM, Donahue TR, Reber HA, Tomlinson JS, et al.
- 976 Long-term survival in patients with pancreatic ductal adenocarcinoma. *Surgery*.
- 977 2016;159:1520–7.
- 978
- 979 2. Kraman M, Bambrough PJ, Arnold JN, Roberts EW, Magiera L, Jones JO, et al.
- 980 Suppression of Antitumor Immunity by Stromal Cells Expressing Fibroblast Activation
- 981 Protein- α . *Science*. 2010;330:827–30.
- 982
- 983 3. Lo A, Wang L-CS, Scholler J, Monslow J, Avery D, Newick K, et al. Tumor-Promoting
- 984 Desmoplasia Is Disrupted by Depleting FAP-Expressing Stromal Cells. *Cancer Res*.
- 985 2015;75:2800–10.
- 986
- 987 4. Özdemir BC, Pentcheva-Hoang T, Carstens JL, Zheng X, Wu C-C, Simpson TR, et
- 988 al. Depletion of Carcinoma-Associated Fibroblasts and Fibrosis Induces
- 989 Immunosuppression and Accelerates Pancreas Cancer with Reduced Survival. *Cancer*
- 990 *Cell*. 2015;28:831–3.
- 991
- 992 5. Santos AM, Jung J, Aziz N, Kissil JL, Puré E. Targeting fibroblast activation protein
- 993 inhibits tumor stromagenesis and growth in mice. *J Clin Invest*. 2009;119:3613–25.
- 994
- 995 6. Wang L-CS, Lo A, Scholler J, Sun J, Majumdar RS, Kapoor V, et al. Targeting
- 996 Fibroblast Activation Protein in Tumor Stroma with Chimeric Antigen Receptor T Cells
- 997 Can Inhibit Tumor Growth and Augment Host Immunity without Severe Toxicity. *Cancer*
- 998 *Immunol Res*. 2014;2:154–66.
- 999
- 1000 7. LeBleu VS, Kalluri R. A peek into cancer-associated fibroblasts: origins, functions and
- 1001 translational impact. *Dis Model Mech*. 2018;11:dmm029447.
- 1002
- 1003 8. Avery D, Govindaraju P, Jacob M, Todd L, Monslow J, Puré E. Extracellular matrix
- 1004 directs phenotypic heterogeneity of activated fibroblasts. *Matrix Biol*. 2018;67.
- 1005
- 1006 9. Costa A, Kieffer Y, Scholer-Dahirel A, Pelon F, Bourachot B, Cardon M, et al.
- 1007 Fibroblast Heterogeneity and Immunosuppressive Environment in Human Breast
- 1008 Cancer. *Cancer Cell*. 2018;33.
- 1009
- 1010 10. Feig C, Jones JO, Kraman M, Wells RJ, Deonaraine A, Chan DS, et al. Targeting
- 1011 CXCL12 from FAP-expressing carcinoma-associated fibroblasts synergizes with anti-
- 1012 PD-L1 immunotherapy in pancreatic cancer. *Proc National Acad Sci*. 2013;110:20212–
- 1013 7.
- 1014
- 1015 11. Apte M, Haber P, Applegate T, Norton I, McCaughan G, Korsten M, et al. Periacinar
- 1016 stellate shaped cells in rat pancreas: identification, isolation, and culture. *Gut*.
- 1017 1998;43:128–33.

- 1018
1019 12. Aguirre AJ, Bardeesy N, Sinha M, Lopez L, Tuveson DA, Horner J, et al. Activated
1020 Kras and Ink4a/Arf deficiency cooperate to produce metastatic pancreatic ductal
1021 adenocarcinoma. *Gene Dev.* 2003;17:3112–26.
1022
1023 13. Chung W-J, Daemen A, Cheng JH, Long JE, Cooper JE, Wang B, et al. Kras mutant
1024 genetically engineered mouse models of human cancers are genomically
1025 heterogeneous. *Proc National Acad Sci.* 2017;114:E10947–55.
1026
1027 14. Hruban RH, Adsay VN, Albores-Saavedra J, Anver MR, Biankin AV, Boivin GP, et
1028 al. Pathology of Genetically Engineered Mouse Models of Pancreatic Exocrine Cancer:
1029 Consensus Report and Recommendations. *Cancer Res.* 2006;66:95–106.
1030
1031 15. Erkan M, Reiser-Erkan C, Michalski CW, Deucker S, Sauliunaite D, Streit S, et al.
1032 Cancer-Stellate Cell Interactions Perpetuate the Hypoxia-Fibrosis Cycle in Pancreatic
1033 Ductal Adenocarcinoma. *Neoplasia.* 2009;11:497–508.
1034
1035 16. Buechler MB, Kim K-W, Onufer EJ, Williams JW, Little CC, Dominguez CX, et al. A
1036 Stromal Niche Defined by Expression of the Transcription Factor WT1 Mediates
1037 Programming and Homeostasis of Cavity-Resident Macrophages. *Immunity.*
1038 2019;51:119-130.e5.
1039
1040 17. Cremasco V, Astarita JL, Grauel AL, Keerthivasan S, MacIsaac KD, Woodruff MC,
1041 et al. FAP delineates heterogeneous and functionally divergent stromal cells in immune-
1042 excluded breast tumors. *Cancer Immunol Res.* 2018;6:canimm.0098.2018.
1043
1044 18. Xie T, Wang Y, Deng N, Huang G, Taghavifar F, Geng Y, et al. Single-Cell
1045 Deconvolution of Fibroblast Heterogeneity in Mouse Pulmonary Fibrosis. *Cell Reports.*
1046 2018;22:3625–40.
1047
1048 19. Street K, Risso D, Fletcher RB, Das D, Ngai J, Yosef N, et al. Slingshot: cell lineage
1049 and pseudotime inference for single-cell transcriptomics. *Bmc Genomics.* 2018;19:477.
1050
1051 20. Kalluri R. Basement membranes: structure, assembly and role in tumour
1052 angiogenesis. *Nat Rev Cancer.* 2003;3:422–33.
1053
1054 21. Groulx J-F, Gagné D, Benoit YD, Martel D, Basora N, Beaulieu J-F. Collagen VI is a
1055 basement membrane component that regulates epithelial cell–fibronectin interactions.
1056 *Matrix Biol.* 2011;30:195–206.
1057
1058 22. Steele CW, Karim SA, Leach J, Bailey P, Upstill-Goddard R, Rishi L, et al. CXCR2
1059 Inhibition Profoundly Suppresses Metastases and Augments Immunotherapy in
1060 Pancreatic Ductal Adenocarcinoma. *Cancer Cell.* 2016;29:832–45.
1061
1062 23. Sano M, Ijichi H, Takahashi R, Miyabayashi K, Fujiwara H, Yamada T, et al.
1063 Blocking CXCLs–CXCR2 axis in tumor–stromal interactions contributes to survival in a

- 1064 mouse model of pancreatic ductal adenocarcinoma through reduced cell
1065 invasion/migration and a shift of immune-inflammatory microenvironment. *Oncogenesis*.
1066 2019;8:8.
1067
- 1068 24. Long KB, Gladney WL, Tooker GM, Graham K, Fraietta JA, Beatty GL. IFN γ and
1069 CCL2 Cooperate to Redirect Tumor-Infiltrating Monocytes to Degrade Fibrosis and
1070 Enhance Chemotherapy Efficacy in Pancreatic Carcinoma. *Cancer Discov*. 2016;6:400–
1071 13.
1072
- 1073 25. Jackson HW, Defamie V, Waterhouse P, Khokha R. TIMPs: versatile extracellular
1074 regulators in cancer. *Nat Rev Cancer*. 2017;17:38.
1075
- 1076 26. Goel H, Mercurio AM. VEGF targets the tumour cell. *Nat Rev Cancer*. 2013;13:871–
1077 82.
1078
- 1079 27. Liang M, Ma Q, Ding N, Luo F, Bai Y, Kang F, et al. IL-11 is essential in promoting
1080 osteolysis in breast cancer bone metastasis via RANKL-independent activation of
1081 osteoclastogenesis. *Cell Death Dis*. 2019;10:353.
1082
- 1083 28. Shi Y, Gao W, Lytle NK, Huang P, Yuan X, Dann AM, et al. Targeting LIF-mediated
1084 paracrine interaction for pancreatic cancer therapy and monitoring. *Nature*.
1085 2019;569:131–5.
1086
- 1087 29. Pietras K, Sjöblom T, Rubin K, Heldin C-H, Östman A. PDGF receptors as cancer
1088 drug targets. *Cancer Cell*. 2003;3:439–43.
1089
- 1090 30. D'Costa Z, Jones K, Azad A, van Stiphout R, Lim SY, Gomes AL, et al.
1091 Gemcitabine-induced TIMP1 attenuates therapy response and promotes tumor growth
1092 and liver metastasis in pancreatic cancer. *Cancer Res*. 2017;77:canres.2833.2016.
1093
- 1094 31. Costa-Silva B, Aiello NM, Ocean AJ, Singh S, Zhang H, Thakur B, et al. Pancreatic
1095 cancer exosomes initiate pre-metastatic niche formation in the liver. *Nat Cell Biol*.
1096 2015;17:816–26.
1097
- 1098 32. Mariathasan S, Turley SJ, Nickles D, Castiglioni A, Yuen K, Wang Y, et al. TGF β
1099 attenuates tumour response to PD-L1 blockade by contributing to exclusion of T
1100 cells. *Nature*. 2018;554:544.
1101
- 1102 33. Ling J, Kang Y, Zhao R, Xia Q, Lee D-F, Chang Z, et al. KrasG12D-Induced
1103 IKK2/ β /NF- κ B Activation by IL-1 α and p62 Feedforward Loops Is Required for
1104 Development of Pancreatic Ductal Adenocarcinoma. *Cancer Cell*. 2012;21:105–20.
1105
- 1106 34. Schmid MC, Avraamides CJ, Foubert P, Shaked Y, Kang S, Kerbel RS, et al.
1107 Combined Blockade of Integrin- α 4 β 1 Plus Cytokines SDF-1 α or IL-1 β Potently Inhibits
1108 Tumor Inflammation and Growth. *Cancer Res*. 2011;71:6965–75.
1109

- 1110 35. Tjomsland V, Bojmar L, Sandström P, Bratthäll C, Messmer D, Spångeus A, et al.
1111 IL-1 α Expression in Pancreatic Ductal Adenocarcinoma Affects the Tumor Cell
1112 Migration and Is Regulated by the p38MAPK Signaling Pathway. *Plos One*.
1113 2013;8:e70874.
1114
- 1115 36. Elyada E, Bolisetty M, Laise P, Flynn WF, Courtois ET, Burkhart RA, et al. Cross-
1116 Species Single-Cell Analysis of Pancreatic Ductal Adenocarcinoma Reveals Antigen-
1117 Presenting Cancer-Associated Fibroblasts. *Cancer Discov*. 2019;9:1102–23.
1118
- 1119 37. Calon A, Espinet E, Palomo-Ponce S, Tauriello D, Iglesias M, Céspedes M, et al.
1120 Dependency of Colorectal Cancer on a TGF- β -Driven Program in Stromal Cells for
1121 Metastasis Initiation. *Cancer Cell*. 2012;22:571–84.
1122
- 1123 38. Purcell JW, Tanlimco SG, Hickson JA, Fox M, Sho M, Durkin L, et al. LRRC15 is a
1124 novel mesenchymal protein and stromal target for antibody-drug conjugates. *Cancer*
1125 *Res*. 2018;78:canres.0327.2018.
1126
- 1127 39. Bausch-Fluck D, Hofmann A, Bock T, Frei AP, Cerciello F, Jacobs A, et al. A Mass
1128 Spectrometric-Derived Cell Surface Protein Atlas. *Plos One*. 2015;10:e0121314.
1129
- 1130 40. Öhlund D, Handy-Santana A, Biffi G, Elyada E, Almeida AS, Ponz-Sarvisé M, et al.
1131 Distinct populations of inflammatory fibroblasts and myofibroblasts in pancreatic cancer.
1132 *J Exp Med*. 2017;214:jem.20162024.
1133
- 1134 41. Peng J, Sun B-F, Chen C-Y, Zhou J-Y, Chen Y-S, Chen H, et al. Single-cell RNA-
1135 seq highlights intra-tumoral heterogeneity and malignant progression in pancreatic
1136 ductal adenocarcinoma. *Cell Res*. 2019;1–14.
1137
- 1138 42. Maurer C, Holmstrom SR, He J, Laise P, Su T, Ahmed A, et al. Experimental
1139 microdissection enables functional harmonisation of pancreatic cancer subtypes. *Gut*.
1140 2019;68:1034.
1141
- 1142 43. Puram SV, Tirosh I, Parikh AS, Patel AP, Yizhak K, Gillespie S, et al. Single-Cell
1143 Transcriptomic Analysis of Primary and Metastatic Tumor Ecosystems in Head and
1144 Neck Cancer. *Cell*. 2017;171:1611-1624.e24.
1145
- 1146 44. Principe DR, Park A, Dorman MJ, Kumar S, Viswakarma N, Rubin J, et al. TGF β
1147 Blockade Augments PD-1 Inhibition to Promote T-Cell Mediated Regression of
1148 Pancreatic Cancer. *Mol Cancer Ther*. 2018;18:molcanther.0850.2018.
1149
- 1150 45. Moffitt RA, Marayati R, Flate EL, Volmar KE, Loeza GS, Hoadley KA, et al. Virtual
1151 microdissection identifies distinct tumor- and stroma-specific subtypes of pancreatic
1152 ductal adenocarcinoma. *Nat Genet*. 2015;47:1168.
1153
- 1154 46. Thorsson V, Gibbs DL, Brown SD, Wolf D, Bortone DS, Yang T-H, et al. The
1155 Immune Landscape of Cancer. *Immunity*. 2018;48:812-830.e14.

- 1156
1157 47. Biffi G, Oni TE, Spielman B, Hao Y, Elyada E, Park Y, et al. IL-1-induced JAK/STAT
1158 signaling is antagonized by TGF-beta to shape CAF heterogeneity in pancreatic ductal
1159 adenocarcinoma. *Cancer Discov.* 2018;CD-18-0710.
1160
1161 48. Koopmans T, Rinkevich Y. Mesothelial to mesenchyme transition as a major
1162 developmental and pathological player in trunk organs and their cavities. *Commun*
1163 *Biology.* 2018;1:170.
1164
1165 49. Corcoran RB, Contino G, Deshpande V, Tzatsos A, Conrad C, Benes CH, et al.
1166 STAT3 Plays a Critical Role in KRAS-Induced Pancreatic Tumorigenesis. *Cancer Res.*
1167 2011;71:5020–9.
1168
1169 50. Shien K, Papadimitrakopoulou VA, Ruder D, Behrens C, Shen L, Kalhor N, et al.
1170 JAK1/STAT3 Activation through a Proinflammatory Cytokine Pathway Leads to
1171 Resistance to Molecularly Targeted Therapy in Non–Small Cell Lung Cancer. *Mol*
1172 *Cancer Ther.* 2017;16:2234–45.
1173
1174 51. Grivennikov SI, Karin M. Dangerous liaisons: STAT3 and NF-κB collaboration and
1175 crosstalk in cancer. *Cytokine Growth F R.* 2010;21:11–9.
1176
1177 52. Fletcher AL, Malhotra D, Acton SE, Lukacs-Kornek V, Bellemare-Pelletier A, Curry
1178 M, et al. Reproducible Isolation of Lymph Node Stromal Cells Reveals Site-Dependent
1179 Differences in Fibroblastic Reticular Cells. *Front Immunol.* 2011;2:35.
1180
1181 53. Morgan-Lappe S, GISH KC, Hickson JA, Purcell JW. ANTI-huLRRC15 ANTIBODY
1182 DRUG CONJUGATES AND METHODS FOR THEIR USE.
1183
1184 54. van den Brink SC, Sage F, Vértesy Á, Spanjaard B, Peterson-Maduro J, Baron CS,
1185 et al. Single-cell sequencing reveals dissociation-induced gene expression in tissue
1186 subpopulations. *Nat Methods.* 2017;14:935–6.
1187
1188 55. Korsunsky I, Fan J, Slowikowski K, Zhang F, Wei K, Baglaenko Y, et al. Fast,
1189 sensitive, and accurate integration of single cell data with Harmony. *Biorxiv.*
1190 2018;461954.
1191
1192 56. Stuart T, Butler A, Hoffman P, Hafemeister C, Papalexi E, Mauck WM, et al.
1193 Comprehensive Integration of Single-Cell Data. *Cell.* 2019;177:1888-1902.e21.
1194
1195 57. Tirosh I, Venteicher AS, Hebert C, Escalante LE, Patel AP, Yizhak K, et al. Single-
1196 cell RNA-seq supports a developmental hierarchy in human oligodendroglioma. *Nature.*
1197 2016;539:309.
1198
1199 58. Herwig R, Hardt C, Lienhard M, Kamburov A. Analyzing and interpreting genome
1200 data at the network level with ConsensusPathDB. *Nat Protoc.* 2016;11:1889–907.
1201

- 1202 59. Huang D, Sherman BT, Tan Q, Collins JR, Alvord GW, Roayaei J, et al. The DAVID
1203 Gene Functional Classification Tool: a novel biological module-centric algorithm to
1204 functionally analyze large gene lists. *Genome Biol.* 2007;8:R183.
1205
- 1206 60. Sui SJ, Mortimer JR, Arenillas DJ, Brumm J, Walsh CJ, Kennedy BP, et al.
1207 oPOSSUM: identification of over-represented transcription factor binding sites in co-
1208 expressed genes. *Nucleic Acids Res.* 2005;33:3154–64.
1209
- 1210 61. Ritchie ME, Phipson B, Wu D, Hu Y, Law CW, Shi W, et al. limma powers
1211 differential expression analyses for RNA-sequencing and microarray studies. *Nucleic
1212 Acids Res.* 2015;43:e47–e47.
1213
- 1214 62. Benjamini Y, Hochberg Y. Controlling the False Discovery Rate: A Practical and
1215 Powerful Approach to Multiple Testing. *J Royal Statistical Soc Ser B Methodol.*
1216 1995;57:289–300.
1217
- 1218 63. Robinson JT, Thorvaldsdóttir H, Winckler W, Guttman M, Lander ES, Getz G, et al.
1219 Integrative genomics viewer. *Nat Biotechnol.* 2011;29:24.
1220
- 1221 64. Müller S, Cho A, Liu SJ, Lim DA, Diaz A. CONICS integrates scRNA-seq with DNA
1222 sequencing to map gene expression to tumor sub-clones. *Bioinformatics.*
1223 2018;34:3217–9.
1224
- 1225 65. Durinck S, Spellman PT, Birney E, Huber W. Mapping identifiers for the integration
1226 of genomic datasets with the R/Bioconductor package biomaRt. *Nat Protoc.*
1227 2009;4:1184.
1228
- 1229 66. Tang Z, Li C, Kang B, Gao G, Li C, Zhang Z. GEPIA: a web server for cancer and
1230 normal gene expression profiling and interactive analyses. *Nucleic Acids Res.*
1231 2017;gkx247-.
1232
- 1233 67. Consortium Gte, Laboratory D, Group S, groups E, Fund N, NIH/NCI, et al. Genetic
1234 effects on gene expression across human tissues. *Nature.* 2017;550:204.
1235
- 1236 68. Rosenberg JE, Hoffman-Censits J, Powles T, van der Heijden MS, Balar AV, Necchi
1237 A, et al. Atezolizumab in patients with locally advanced and metastatic urothelial
1238 carcinoma who have progressed following treatment with platinum-based
1239 chemotherapy: a single-arm, multicentre, phase 2 trial. *Lancet.* 2016;387:1909–20.
1240
- 1241 69. Kowanetz M, Zou W, Gettinger SN, Koeppen H, Kockx M, Schmid P, et al.
1242 Differential regulation of PD-L1 expression by immune and tumor cells in NSCLC and
1243 the response to treatment with atezolizumab (anti-PD-L1). *Proc National Acad Sci.*
1244 2018;115:201802166.
1245
1246

1247 **FIGURE LEGENDS**

1248 **Figure 1. Podoplanin (PDPN) expression identifies the majority of tissue**
1249 **fibroblasts in normal and tumor-bearing pancreas. a)** PDPN and CD31 expression
1250 on cells digested according to standard stellate cell pronase protocols (left) or new
1251 digestion protocol (right) and enriched by gradient centrifugation, gated on live CD45⁻
1252 Epcam⁻ cells. **b)** PDPN and CD31 expression in normal or tumor-bearing KPP GEMM
1253 pancreases (left) with quantification (right). Blood endothelial cells (BECs) are PDPN-
1254 CD31⁺ as highlighted in the contour plots (green). **c)** Immunofluorescence imaging of
1255 PDPN staining in normal pancreas (left, arrowheads highlight examples of PDPN⁺ cells
1256 surrounding acinar clusters) and KPP GEMM in advanced PDAC, either in “distal” tissue
1257 not directly contacting tumor (middle) or “proximal” where tumor cells were visibly
1258 contacting non-tumor tissue (right). Scale bar represents 50um. **d)** Heatmap showing
1259 relative gene expression levels from RNA-seq analysis of PDPN⁺CD31⁻PDGFRa⁺
1260 stroma and the DN populations demonstrating fibroblastic nature of the PDPN⁺
1261 population. **e)** Expression of selected CAF-associated genes in respective fibroblasts
1262 populations (log₂(rPKM+1)). Statistical comparison between all groups performed with
1263 Tukey's test, bars designate pairwise comparisons where p<.05. All dot plots are
1264 representative of flow cytometry data from single-cell dissociated tissues. a) is
1265 representative of 4 independent experiments with 5 animals pooled per condition. b)
1266 Combined data from 5 independent experiments with total n=12 for normal and n=25 for
1267 PDAC GEMM. Statistical test used was Sidak's multiple comparisons test ***p<0.0005;
1268 **** p<0.0001 c) Representative image from normal n=4 for PDAC GEMMs n= 10. d) for
1269 normal samples n=3-4, with 5 animals pooled/single sequenced sample, for tumor n=4
1270 with 1-2 animals pooled/single sequenced sample.

1271
1272 **Figure 2. PDPN expression is a feature of several stromal populations. a)**
1273 Experimental design of the scRNA-seq experiment. **b)** Left: t-Distributed Stochastic
1274 Neighbor Embedding (tSNE) embedding of 13,454 single cells sorted from n=20 mice
1275 across all conditions (normal, adjacent, small and large tumors). Clusters identified
1276 through graph-based clustering are indicated by color. Right: Heatmap showing the
1277 relative average expression of the most strongly enriched genes for each cluster

1278 identified by log-fold change of cells within a cluster to all other cells in the dataset. Two
1279 representative genes are highlighted for each cluster. fEMT: full EMT, pEMT: partial
1280 EMT. **c)** tSNE embedding as in b), color indicates normalized expression level
1281 ($\log(\text{CPM}/100+1)$) of indicated genes. **d)** Fraction of cells in each cluster (z-scored per
1282 row) from each condition (column). Two adjacent rows per cluster visualize the fraction
1283 in each replicate. **e)** Left: Comparison of gene expression from bulk RNA-seq data
1284 between normal mesothelial cells and fibroblasts based on \log_2 fold-change (x-axis)
1285 and $-\log_{10}(\text{adj. p-value; limma})$. Genes enriched in cluster 6 of the scRNA-seq data in
1286 Fig. 2b are highlighted in red, genes upregulated in clusters 3 and 4 are highlighted in
1287 green. Right: Heatmap of the relative average expression of markers for mesothelial
1288 cells identified by both Xie et al. (scRNA-seq) and Buechler et al. (bulk RNA-seq) in
1289 clusters 0,1,2,3,4,6, and 8 from b). **f)** The fraction of fibroblast cells from clusters 0, 2, 8,
1290 and 1 (y-axis) in tumor adjacent tissue, tissue from small, and tissue from large tumors
1291 (x-axis; columns sum to 1).

1292

1293 **Figure 3. Two normal tissue fibroblasts follow two separate differentiation**
1294 **trajectories driven by IL1 and TGFB. a)** Left: UMAP embedding of cells from normal
1295 pancreas. Color and numbers indicate dot density
1296 (grey:low;blue:low/medium;/red:medium/high;yellow:high). Middle: Color indicates
1297 cluster membership. Right: Color indicates marker gene expression. **b)** Representative
1298 flow cytometry plots of fibroblasts gated on live PDPN⁺ fibroblasts from normal mouse
1299 pancreas stained for DPP4 and ENDOGLIN (ENG) or Ly6c and ENG. **c)** Top: Density
1300 distribution of cells from individual fibroblast clusters (color) along the first principal
1301 component of a PCA analysis. Bottom: PC1 loadings of genes highlighted in Suppl. Fig.
1302 3a. **d)** Left: tSNE from Fig. 2b) restricted to fibroblasts. Color indicates the score for
1303 expression of marker genes for two populations from normal pancreas shown in a.
1304 Right: Boxplots outline the distribution of scores in each cluster. **e)** Heatmap visualizing
1305 the relative average expression of indicated genes (rows) in fibroblast clusters
1306 (columns). **f)** Top: Monocle2 pseudo-time trajectory of c4 normal fibroblasts and c4-
1307 derived CAFs. Cells are colored by cluster. Bottom: same as top, but for c3 normal
1308 fibroblasts and c3-derived CAFs. **g)** Heatmaps visualizing the relative average

1309 expression of extracellular matrix encoding genes (top) and chemokines/cytokines
1310 (bottom) across the 6 main fibroblast clusters (rows). Columns were clustered using
1311 complete linkage clustering and Euclidean distance as distance measure. **h)** Left:
1312 Transcription factor motif enrichment analysis in promoters (± 10 kb of TSS) of genes
1313 specific to CAF populations c2 and c8. Right: Pathway enrichment analysis for genes
1314 specific to CAF clusters 8 (top) and 2 (bottom). **i)** Left: Heatmap visualizing the relative
1315 average expression of genes from the F-TBRS signature across fibroblast clusters.
1316 Columns were clustered with complete linkage clustering using Euclidean distance.
1317 Right: Relative average expression of indicated genes (columns) in CAF clusters (rows).
1318 Columns were clustered with complete linkage clustering using Euclidean distance. **j)**
1319 Heatmap comparing the relative average expression of markers genes (rows) of normal
1320 fibroblast clusters 3 and 4, as well as normal mesothelial cells between iCAFs,
1321 myCAFs, apCAFs, c3 normal fibroblasts, c4 normal fibroblasts, and normal mesothelial
1322 cells (rows). Rows and columns were clustered with complete linkage clustering using
1323 Euclidean distance as distance measure.

1324

1325 **Figure 4. TGFB-responsive CAF can be identified by LRRC15 expression.** **a)** Log₂
1326 fold-change of gene expression (dots) between normal fibroblasts and early PDPN⁺
1327 PDAC CAFs (x-axis) and normal fibroblasts and late-stage PDAC CAFs (y-axis). Genes
1328 significant (adj. p-val<0.1 and absolute(log₂FC)>1) are indicated in blue, genes
1329 significant in only late stage CAFs in green and only in early CAFs in red. **b)**
1330 Immunofluorescent image of PDPN (green), LRRC15 (white), EPCAM (red), and DAPI
1331 (blue) expression in tumor-bearing KPP GEMM pancreas, yellow arrowheads highlight
1332 examples of LRRC15⁺ clusters. **c)** Immunofluorescent image of PDPN (green), LRRC15
1333 (white), EPCAM (red), and DAPI (blue) expression in subcutaneous KPP tumor showing
1334 PDPN⁺LRRC15⁺ fibroblasts. **d)** Representative plot showing LRRC15 staining by flow
1335 cytometry in the PDPN⁺ fibroblast gate (left), quantification of LRRC15⁺ cells by
1336 frequency of population and numbers normalized to weight in the KPPsc model. **e)** Top:
1337 Representative images from single wells (from 24-well plate) of KPP-mApple spheroids
1338 after 12 days of 3D culture. KPP-mApple spheroids were cultured alone or co-cultured
1339 with the designated fibroblast population. Bottom: Quantification of total area of mApple⁺

1340 spheroids per whole well over time. These data are combined from 2 independent
1341 experiments, for each experiment n=4 wells/condition. Dunnett's multiple comparison
1342 test, comparing tumor alone against all other conditions, showed a significant difference
1343 ****p<.0001 for all conditions.

1344

1345 **Figure 5. TGFB-responsive LRRC15⁺ CAFs are the most frequent fibroblast**
1346 **population in human PDAC. a)** Left: UMAP embedding of 84,276 high-quality cells
1347 from 22 PDAC patients. Clusters identified through graph-based clustering are indicated
1348 by color. Cells with identified KRAS single-nucleotide variation identified from scRNA-
1349 seq reads are highlighted in orange. Labels for each cluster were identified by markers
1350 on the right. Right: Heatmap showing the relative average expression of the most
1351 strongly enriched genes for each cluster identified by log-fold change of cells within a
1352 cluster to all other cells in the dataset. Two representative genes are highlighted for
1353 each cluster. **b)** Bar plots representing the number of patients that contributed at least
1354 10 cells to a cluster given in a). **c)** Relative expression of marker genes for clusters 0, 5,
1355 and 6 from a) in bulk RNA-seq samples from microdissected tumor (n=65), stroma (n=
1356 122) and normal pancreas (n=247). **d)** Left: UMAP embedding of 8,931 fibroblast cells.
1357 Clusters identified through graph-based clustering are indicated by color. Right:
1358 Heatmap showing the most strongly enriched genes for each cluster identified by
1359 Wilcoxon's ranks sum test, all p<1e-10. Three representative genes are highlighted for
1360 each cluster. **e)** Distribution of left: *LRRC15* and right: *HAS1* expression in bulk RNA-
1361 seq data from 65 tumor, 122 stroma, and 247 normal samples. **f)** Average expression
1362 (+/- standard error of mean) of signature genes from d) in 122 microdissected PDAC
1363 stroma bulk RNA-seq samples. **g)** Representative IHC image from a PDAC patient
1364 sample (1 of 70. More images in Suppl. Fig. 5b). Purple: LRRC15 staining Blue: Nuclear
1365 counterstain Brown: CD8 stain. Dashed line demarcates tumor islet. Arrowheads point
1366 of CD8 T cells. Scale bar represents 200um. **h)** Representative flow cytometry plots of
1367 mesenchymal cells, gated on live EPCAM⁻ CD45⁻ CD31⁻ cells from PDAC tissue
1368 stained for LRRC15 and EPCAM. **i)** Heatmap visualizing the relative average
1369 expression of mouse IL1 CAF markers and mouse TGFB CAF markers and their
1370 respective homologues in human across human and mouse IL1 CAFs, human and

1371 mouse normal fibroblasts, as well as human and mouse TGFB CAFs (rows). Rows and
1372 columns were clustered using complete linkage clustering and Euclidean distance as
1373 distance measure. Representative genes for each of the two main clusters are
1374 highlighted and represented by their human gene symbol. **j)** Top: Scatter plot comparing
1375 the average expression of genes in fibroblast single-cell cluster 5 from normal pancreas
1376 (Suppl. Fig. 5d) to the average expression of CAF cluster 1 from d). Bottom: Heatmap
1377 visualizing the relative average expression of indicated genes (rows) in mouse CAF
1378 clusters from figure 2b). Columns were clustered using complete linkage clustering and
1379 Euclidean distance as distance measure. **k)** Principle component analysis of normal
1380 fibroblasts from Suppl. Figure 5d in purple and human CAFs colored by clusters from d).
1381 Dots and dashed lines represent the cluster-based minimum spanning tree. **l)**
1382 Schematic representation of mouse and human PDAC fibroblast evolution. Rectangles
1383 demarcate different stages of tumor progression; purple is the non-malignant stage*,
1384 orange is the early stage of tumor development, red is the established tumor stage.
1385 Proteins shown have been validated as markers that identify the respective population,
1386 genes that are shown were among the most significantly enriched for that population.
1387 Currently we cannot identify all populations by protein markers. The pie charts show the
1388 frequency of CAF populations found in late tumors for mouse, and overall in patient
1389 PDAC tumor samples based on the scRNA-seq experiments described in Figs. 2 and 5.
1390 *in mice this is the normal tissue baseline, in human the control tissues come from
1391 patients with either duodenal tumors, bile duct tumors, or non-malignant pancreatic
1392 tumors that were scored by a pathologist to have “no visible inflammation”(41)

1393

1394 **Figure 6. Pan-Cancer analysis identifies LRRC15⁺ CAFs as a frequent population**
1395 **across several human tumor types. a)** Distribution of *LRRC15* expression (Log2
1396 TPM) across indicated cancer types (TCGA, n=4,848) compared to their host tissues
1397 (GTEx, n=2,810). **b)** Top: Expression of the 14 most significantly enriched (Wilcoxon’s
1398 rank sum test <1e-285) genes in TGFB CAF cluster 0 compared to cluster 1 as well as
1399 cluster 2 from figure 5d) that are expressed by less than 10 percent of the other cells in
1400 the complete PDAC single-cell dataset. Bottom: Relative average expression in CAF
1401 clusters from Figure 5d). **c)** Relative expression of genes from b) in 122 microdissected

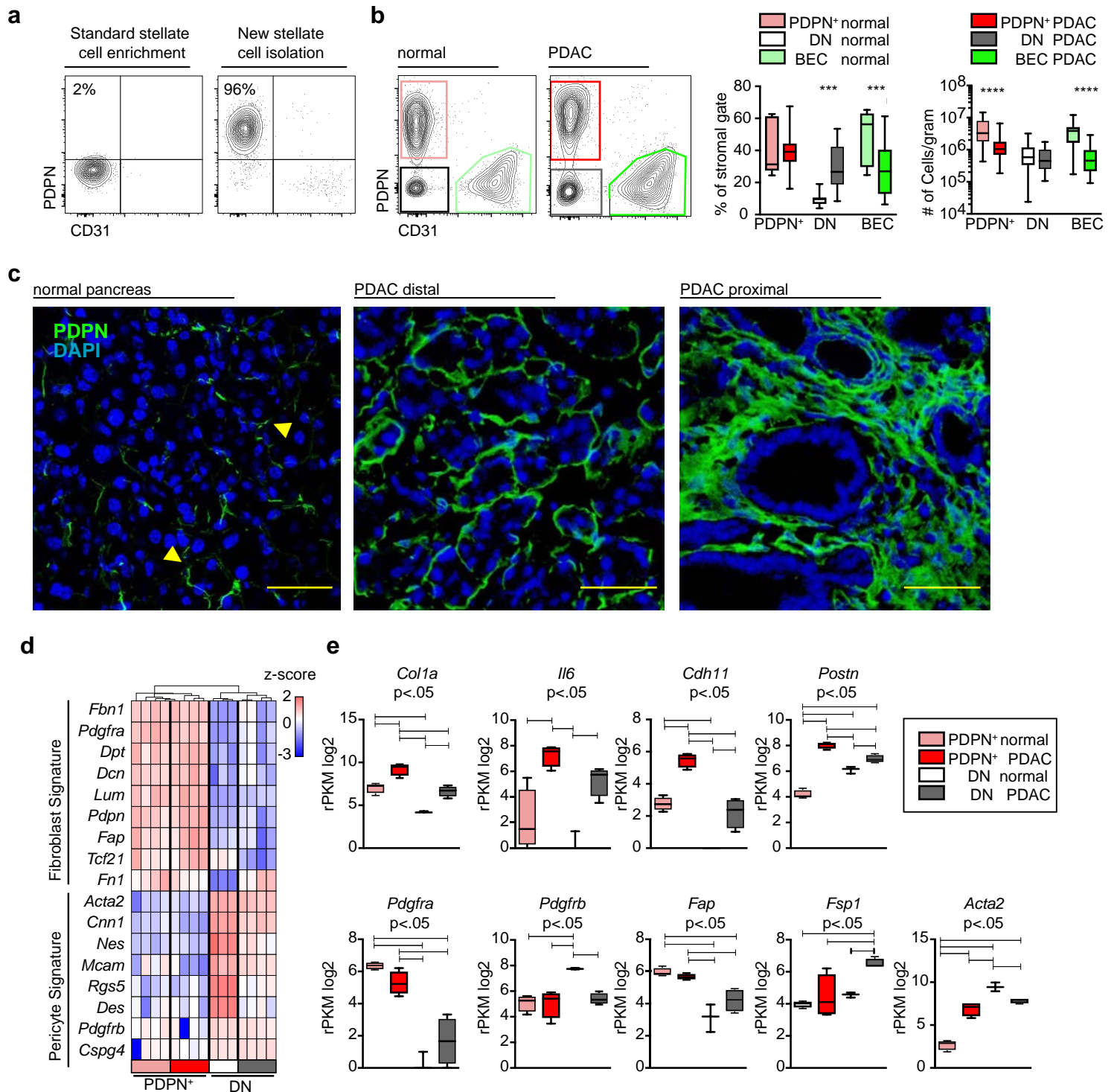
1402 stroma and 65 microdissected tumor samples. **d)** Top left: UMAP embedding of 3,363
1403 non-malignant cells from 18 HNSC biopsies. Cell type assignments provided by the
1404 authors are indicated by color. Top right: UMAP reduction as on the left, colored by
1405 expression ($\text{Log}(\text{CPM}/10+1)$) of indicated genes. Bottom left: UMAP as on top, clusters
1406 identified through graph-based clustering are indicated by color. Bottom right: Heatmap
1407 visualizing the relative average expression of indicated genes (rows) in clusters given
1408 on the bottom left. **e)** Top: Gene-by gene correlation matrix visualizing the pairwise
1409 Spearman's correlation coefficients in bulk RNA-seq TCGA data from pancreatic cancer
1410 (left, $n=178$) and uveal melanoma (right, $n=80$) patients. Bottom: Scatter plot comparing
1411 the average pairwise correlations (x-axis) and average expression (y-axis) of genes
1412 from given on top across 31 cancer indication from TCGA (Total of 9,712 samples from
1413 primary tumors, regression line in blue).

1414

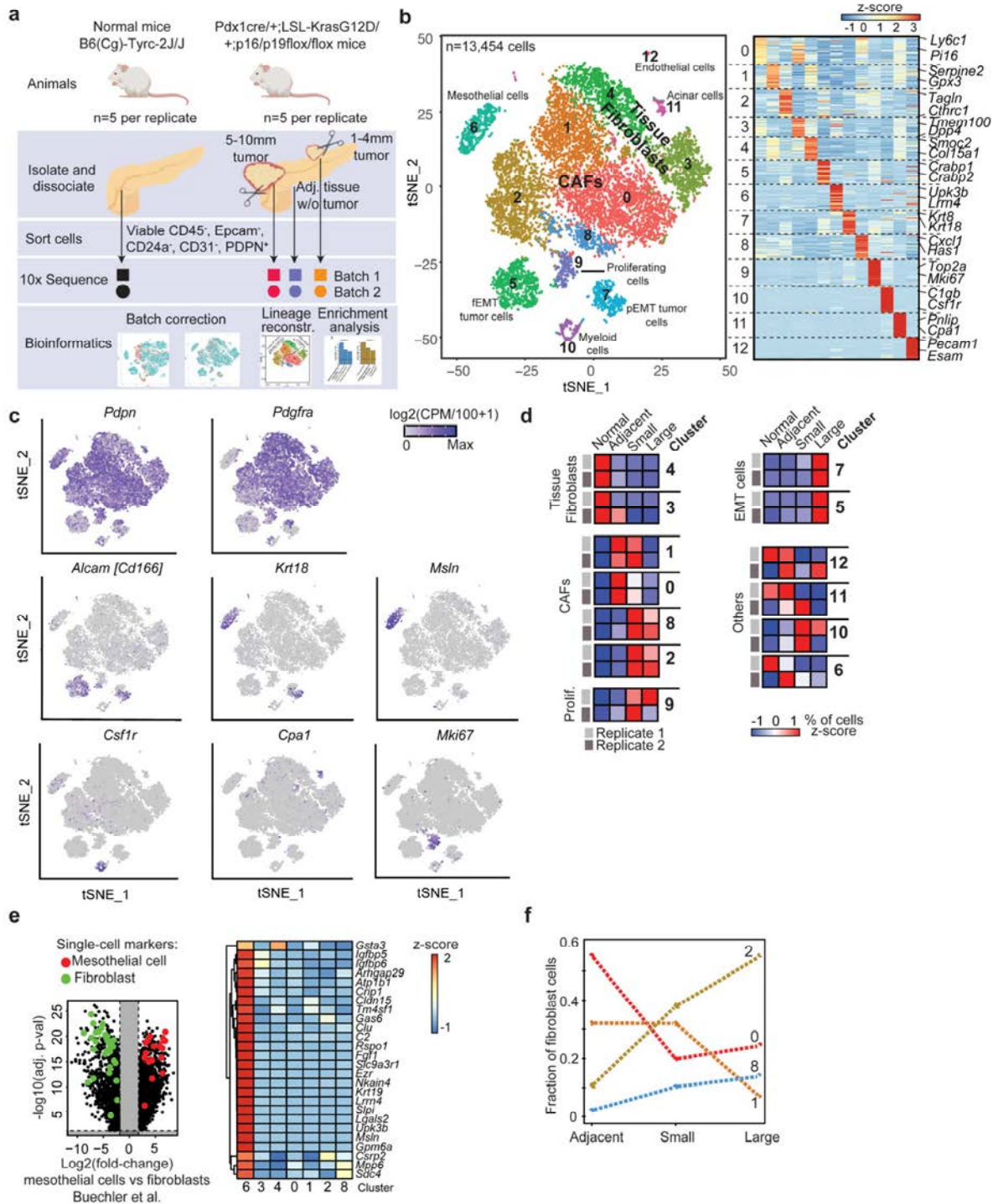
1415 **Figure 7. *LRRC15* expression and its transcriptional signature predicts response**
1416 **to immunotherapy. a)** Boxplots comparing the distribution of the TGFB CAF (top) in
1417 excluded, inflamed and desert tumors from imvigor 210 between responders and non-
1418 responders. *** $p<0.001$, two-sided t-test; CR: Complete Response, PR: Partial
1419 Response, SD: Stable Disease, PD: Progressive disease **b)** Kaplan-Meier survival plot
1420 comparing survival probability (y-axis) and Follow-Up time for 134 patients with locally
1421 advanced or metastatic urothelial carcinoma (imvigor 210) receiving Atezolizumab
1422 treatment, restricted to tumors with excluded immune phenotype. Groups were split by
1423 high (red) or low (green) levels of TGFB CAF marker gene signature expression
1424 (median cutoff). **c)** Boxplots comparing the distributions of pairwise correlations of
1425 genes from the TGFB CAF and the F-TBRS signature in imvigor210 bulk RNA-seq data.
1426 **d)** Survival plot as in b), but here with a score based on the F-TBRS signature genes. **e)**
1427 Kaplan-Meier survival plot comparing survival probability (y-axis) and Follow-Up time for
1428 128 patients from the pcd trial receiving Atezolizumab treatment. Groups were split by
1429 high (red) or low (green) levels of TGFB CAF marker gene signature expression
1430 (>upper vs <lower quartile).

1431

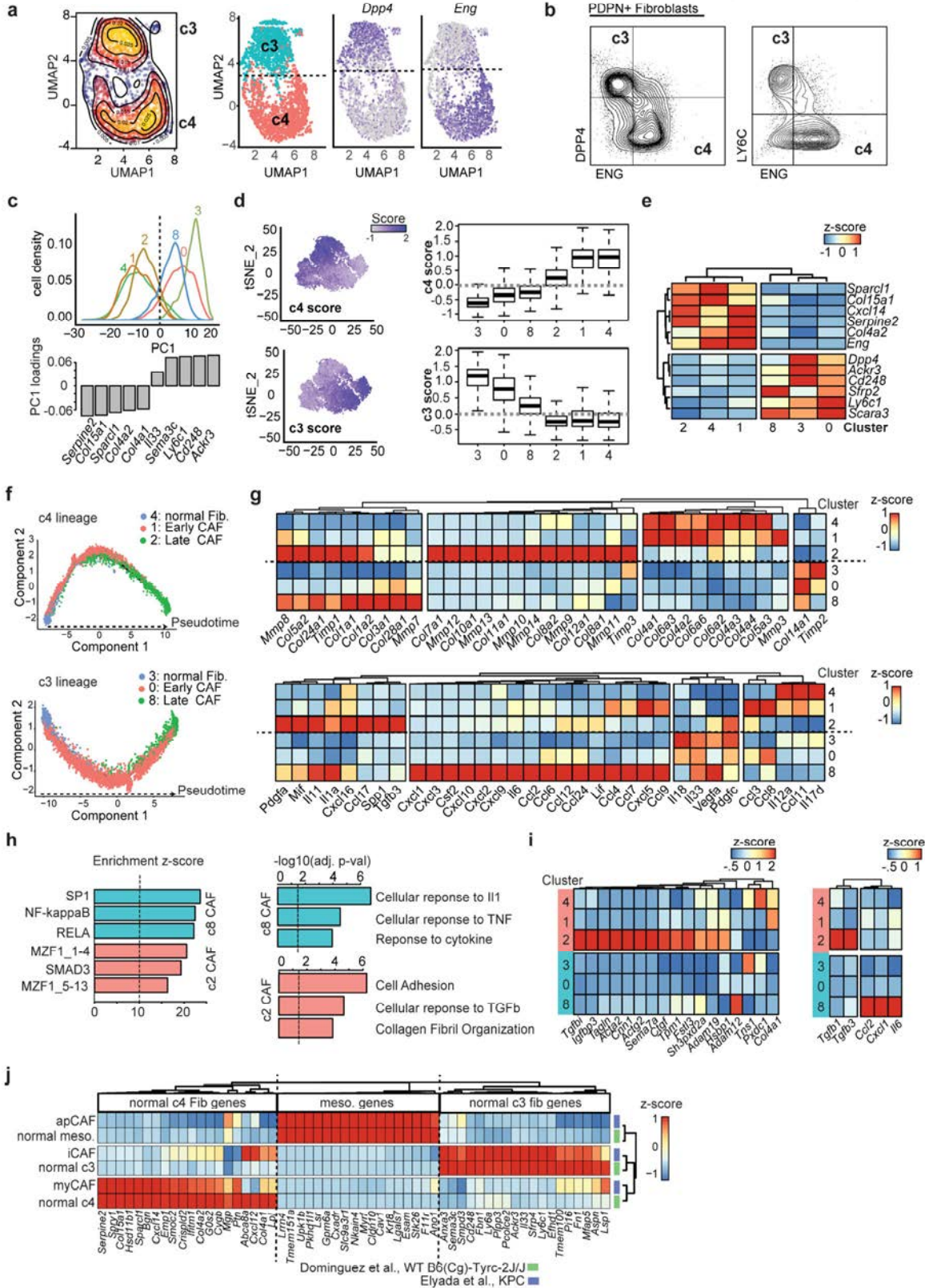
Author Manuscript Published OnlineFirst on November 7, 2019; DOI: 10.1158/2159-8290.CD-19-0644
 Author manuscripts have been peer reviewed and accepted for publication but have not yet been edited.

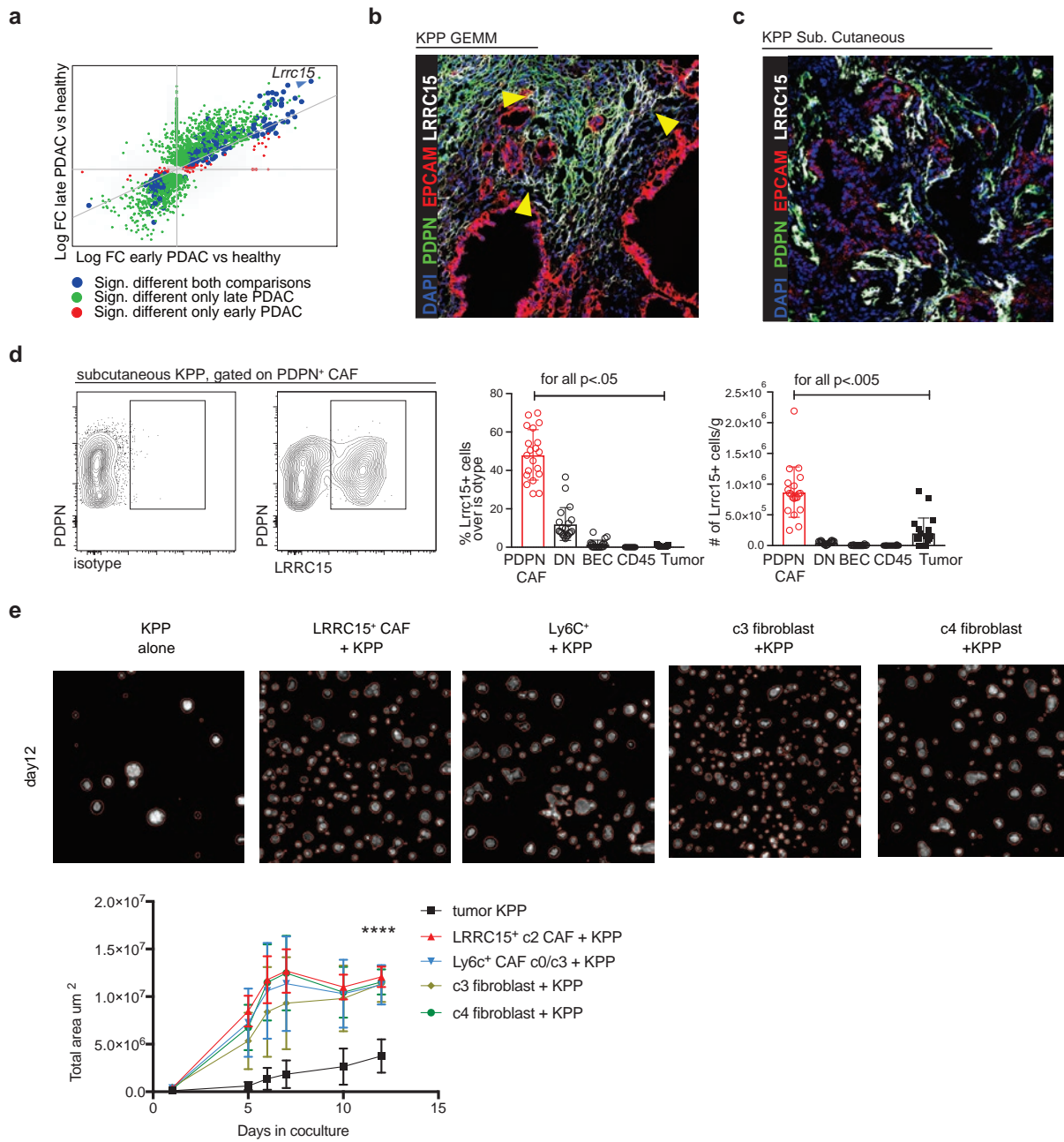


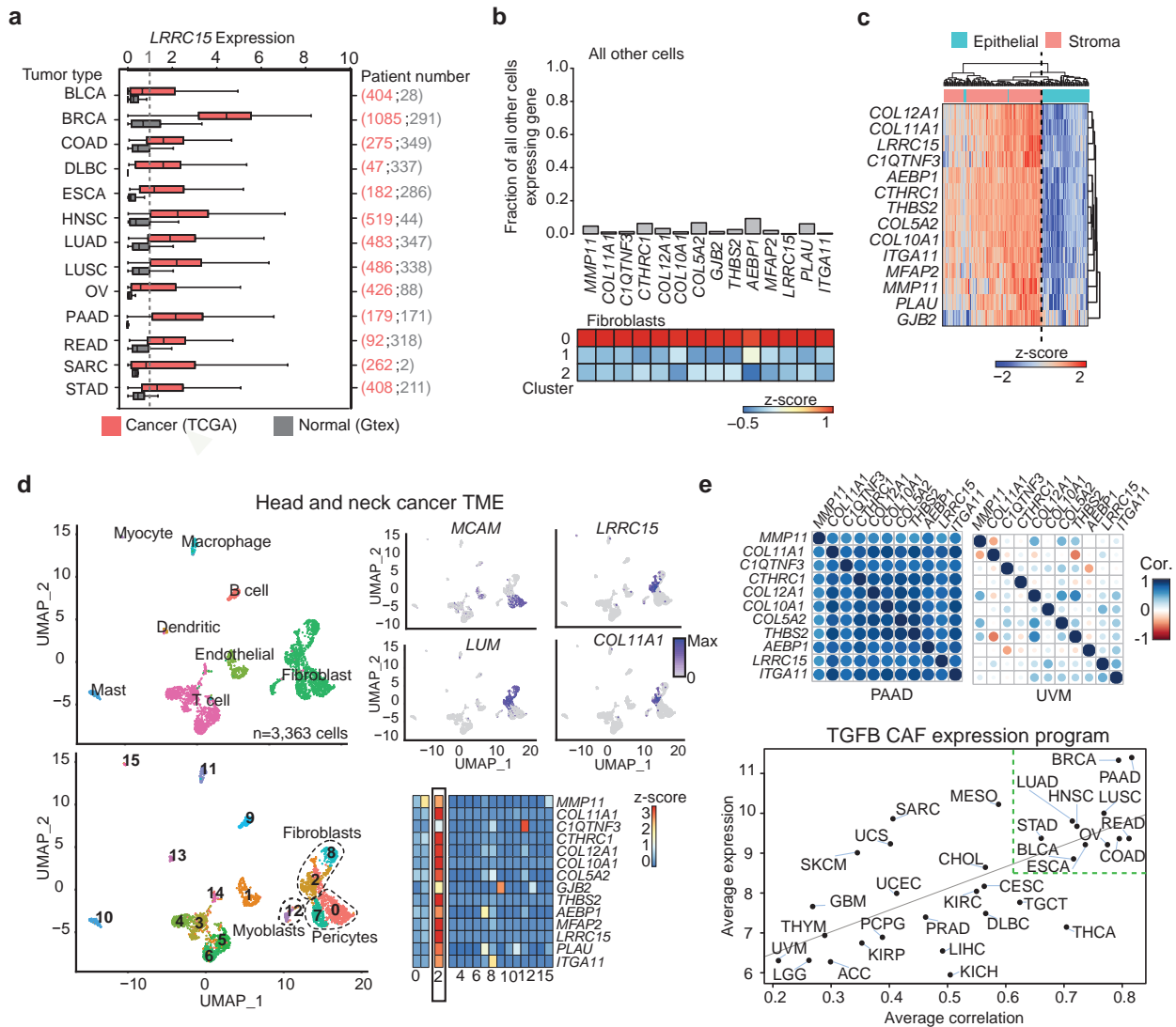
Dominguez, et al., Figure 2

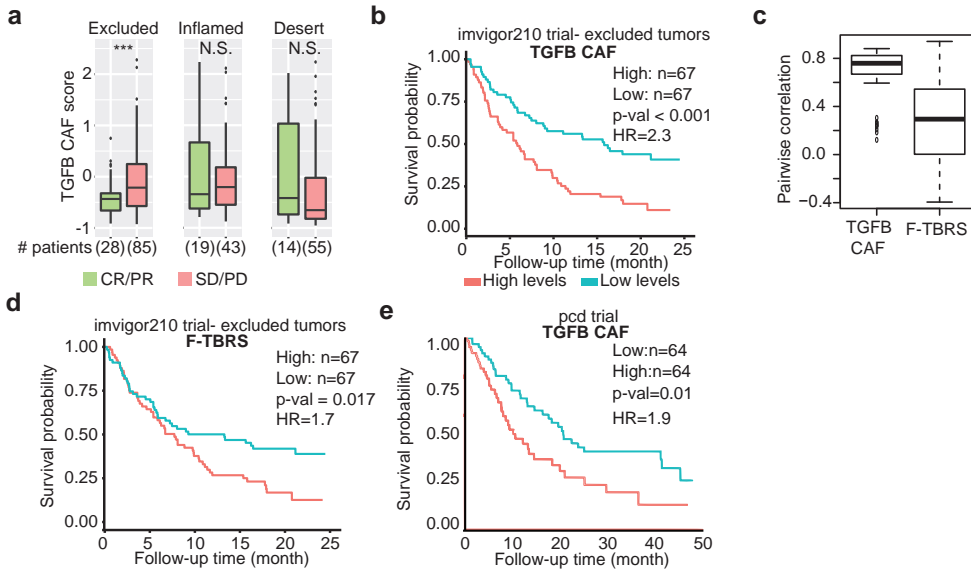


Dominguez, et al., Figure 3









CANCER DISCOVERY

Single-cell RNA sequencing reveals stromal evolution into LRRC15+ myfibroblasts as a determinant of patient response to cancer immunotherapy

Claudia X Dominguez, Soren Muller, Shilpa Keerthivasan, et al.

Cancer Discov Published OnlineFirst November 7, 2019.

Updated version	Access the most recent version of this article at: doi: 10.1158/2159-8290.CD-19-0644
Supplementary Material	Access the most recent supplemental material at: http://cancerdiscovery.aacrjournals.org/content/suppl/2019/11/07/2159-8290.CD-19-0644.DC1
Author Manuscript	Author manuscripts have been peer reviewed and accepted for publication but have not yet been edited.

E-mail alerts	Sign up to receive free email-alerts related to this article or journal.
Reprints and Subscriptions	To order reprints of this article or to subscribe to the journal, contact the AACR Publications Department at pubs@aacr.org .
Permissions	To request permission to re-use all or part of this article, use this link http://cancerdiscovery.aacrjournals.org/content/early/2019/12/13/2159-8290.CD-19-0644 . Click on "Request Permissions" which will take you to the Copyright Clearance Center's (CCC) Rightslink site.